Evolution of Slantwise Vertical Motions in NCEP's Mesoscale Eta Model

MUKUT B. MATHUR AND KEITH F. BRILL

National Centers for Environmental Prediction, Washington, D.C.

CHARLES J. SEMAN

Geophysical Fluid Dynamics Laboratory, Princeton, New Jersey

ABSTRACT

Numerical forecasts from the National Centers for Environmental Prediction's mesoscale version of the η coordinate–based model, hereafter referred to as MESO, have been analyzed to study the roles of conditional symmetric instability (CSI) and frontogenesis in copious precipitation events. A grid spacing of 29 km and 50 layers are used in the MESO model. Parameterized convective and resolvable-scale condensation, radiation physics, and many other physical processes are included. Results focus on a 24-h forecast from 1500 UTC 1 February 1996 in the region of a low-level front and associated deep baroclinic zone over the southeastern United States. Predicted precipitation amounts were close to the observed, and the rainfall in the model was mainly associated with the resolvable-scale condensation.

During the forecast deep upward motion amplifies in a band oriented west-southwest to east-northeast, nearly parallel to the mean tropospheric thermal wind. This band develops from a sloping updraft in the low-level nearly saturated frontal zone, which is absolutely stable to upright convection, but susceptible to CSI. The updraft is then nearly vertical in the middle troposphere where there is very weak conditional instability. We regard this occurrence as an example of model-produced deep slantwise convection (SWC). Negative values of moist potential vorticity (MPV) occur over the entire low-level SWC area initially. The vertical extent of SWC increases with the lifting upward of the negative MPV area. Characteristic features of CSI and SWC simulated in some high-resolution nonhydrostatic cloud models also develop within the MESO. As in the nonhydrostatic SWC, the vertical momentum transport in the MESO updraft generates a subgeostrophic momentum anomaly aloft, with negative absolute vorticity on the baroclinically cool side of the momentum anomaly where outflow winds are accelerated to the north.

Contribution of various processes to frontogenesis in the SWC area is investigated. The development of indirect circulation leads to low-level frontogenesis through the tilting term. The axis of frontogenesis nearly coincides with the axis of maximum vertical motion when the SWC is fully developed. Results suggest that strong vertical motions in the case investigated develop due to release of symmetric instability in a moist atmosphere (CSI), and resultant circulations lead to weak frontogenesis in the SWC area.

1. Introduction

Various mechanisms have been considered to explain the mesoscale organization of precipitation in the form of rainbands in midlatitudes (e.g., see Parsons and Hobbs 1983). In some instances the rainbands are aligned along the thermal wind, and conditional symmetric instability (CSI) theory (Bennetts and Hoskins 1979; Emanuel 1983a) has been applied to explain the formation of such bands (Bennetts and Sharp 1982;

Emanuel 1983b; Seltzer et al. 1985). Ascending motion in such bands occurs nearly along the sloping moist isentropes (Bennetts and Hoskins 1979; Emanuel 1983a). Frontogenetical forcing has also been investigated as a mechanism for enhancing slantwise vertical motions in symmetrically unstable regions (Emanuel 1985; Sanders and Bosart 1985). Our main purpose here is to investigate the role of CSI and frontogenesis in the development of slantwise vertical motions in a prediction from the operational mesoscale model (MESO) of the National Centers for Environmental Prediction (NCEP).

A complete diagnosis of moist symmetric instability entails evaluation of moist potential vorticity (MPV, see section 2 for a definition). Vertical and horizontal gradients of wind and equivalent potential temperature are needed for evaluating the MPV distribution, and these gradients vary substantially in both space and time in

Corresponding author address: Dr. Mukut B. Mathur, NCEP/Environmental Modeling Center, W/NP22, Rm 205, WWBG, NOAA, 5200 Auth Rd, Camp Springs, MD 20746-4304.
E-mail: wd23mm@sgi79.wwb.noaa.gov

mesoscale convective areas. In particular, the equivalent potential temperature gradients vary considerably in the vertical, and these gradients may change significantly, for instance, during the slantwise convective adjustment. Thus, data with high spatial resolution at short time intervals are needed. Both high vertical and horizontal resolution are used in MESO and the predicted fields can be saved at desired time intervals (see section 2). Therefore, data from MESO are well suited for studying symmetric instability. We have found that the distribution of MPV using a vertical spacing of 25 mb (spacing used in our study, see section 2) is often different from that evaluated using a lower resolution (e.g., 200 mb). Note that in many previous observational and numerical studies of symmetric instability, data with lower spatial and time resolutions were utilized. As an example, Bennetts and Sharp (1982) used a 10-level numerical model with a horizontal resolution of 100 km. Seltzer et al. (1985) utilized geostrophic absolute vorticity from a low (vertical and horizontal) resolution analysis and observed soundings to evaluate symmetric instability. Later studies such as Knight and Hobbs (1988), Persson and Warner (1991), and Lindstrom and Nordeng (1992) showed that high model resolution is important for simulating CSI or slantwise convection (SWC).

The organization of the paper is as follows. An overview of the MESO and diagnostic procedures employed is given in section 2. Time evolution of the horizontal structure in the SWC area in a MESO forecast is presented in section 3. Development of SWC employing vertical cross sections of various fields including MPV and condensational heating is discussed in section 4. The case discussed here was selected because the observed significant precipitation amounts over a large area were predicted well, and the following criteria for CSI, which include those discussed in Seltzer et al. (1985), were satisfied (see sections 3–4).

1) The atmospheric conditions in the vicinity of the precipitation bands should be approximately two-dimensional, with larger variations in thermodynamic and kinematic properties in the cross-band and vertical directions.
2) There should be a region of negative MPV in the vicinity of the developing bands (Bennetts and Hoskins 1979; Emanuel 1983a,b).
3) The bands should be oriented approximately parallel to the thermal wind and strongest in the region of instability (Stone 1966, 1970; Busse and Chen 1981; Antar and Fowlis 1983; Miller and Antar 1986).
4) The mesoscale updrafts should be relatively narrow (Xu 1986) and slanted from the vertical (Emanuel 1983a; Seman 1994), and if the atmosphere is saturated should be oriented approximately along surfaces of equivalent potential temperature θ_e (Bennetts and Hoskins 1979; Emanuel 1983a).
5) CSI and slantwise convection theory implies that the

developing precipitation bands should not propagate relative to the mean flow in the cross-band direction (Xu 1986), or have very slow cross-band propagation toward the warm air (Seman 1994). Rapid propagation of precipitation bands would warrant investigation of gravity wave mechanisms (see, e.g., Stobie et al. 1983; Einaudi et al. 1987; Koch et al. 1988; Schneider 1990).
6) Frontogenesis and upper-level jet streak forcings should be weak, as these processes can also generate precipitation bands (Ley and Peltier 1978; Bosart and Sanders 1986; Uccellini and Koch 1987).

In the case presented in this paper, a single slanted mesoscale updraft develops at low levels in a stably stratified region with negative MPV, on the baroclinically cool side of a weak surface cold front. The precipitation pattern develops a quasi-linear two-dimensional structure approximately parallel to the mean tropospheric thermal wind, with centers of strong upward motion in the associated vertical motion field (section 3). Development of distinct mesoscale updrafts in CSI precipitation bands has been previously documented (Seltzer et al. 1985; Lindstrom and Nordeng 1992) and is consistent with the theory of Xu (1986). It will be shown in section 4 that the vertical transport of horizontal momentum creates adjacent regions of inertial instability and stability in the upper troposphere similar to those simulated in the idealized two-dimensional integrations (Seman 1994; Blanchard et al. 1998), and this development causes a significant modification of divergence and creates mesoscale perturbations in the jet streak. In section 5, the distribution of diabatic and other frontogenetical forcing terms is discussed. Additional results are given in section 6, and our conclusions appear in section 7.

2. Methodology

Numerical predictions mainly from the fine (MESO) and coarse (Eta) mesh versions of the η coordinate–based model of NCEP are currently utilized as guidance to produce short-range weather forecasts (up to 48 h) over the United States and adjoining areas. The η coordinate is defined in Mesinger (1984). Both models use a primitive set of equations. A grid spacing of 29 (48) km and 50 (38) layers are presently utilized in the operational MESO (Eta) model.[1] The domains of both models extend over and beyond the U.S. mainland, and the MESO domain is a subset of the Eta domain. The lateral boundary conditions are updated in both models using the forecasts from the AVIATION (global) model of NCEP. The initial conditions for Eta and MESO are

---

[1] NCEP has replaced Eta and MESO with a 45-layer version of MESO with 32-km horizontal grid spacing that is integrated four times daily, beginning on 3 June 1998.

obtained with the use of a Regional Data Assimilation System (RDAS). The analysis from NCEP's Global Data Assimilation System (GDAS) is used as a first guess for the analysis at the initial time of both Eta and MESO RDAS. An overview of the global forecast model and GDAS is provided in Kanamitsu (1989), and RDAS is described in Rogers et al. (1996). The RDAS data assimilation procedure consists of producing a 3-h forecast from an analysis, and utilizing this forecast as a first guess for the next analysis. The Eta RDAS is carried over a 12-h period. As an example, the 0000 UTC GDAS analysis is used in Eta RDAS to produce the initial conditions for the Eta model forecast beginning at 1200 UTC of the same day. The MESO RDAS is performed over a 3-h interval. As an example, the GDAS 1200 UTC analysis is used in MESO RDAS to produce initial conditions for the MESO forecast beginning at 1500 UTC of the same day. The data cutoff time for MESO is later than for Eta. Except for the above differences in the resolution, domain, and initial conditions, the prediction programs of the two models are the same.

Many physical processes, including the convective parameterization based on a modified Betts–Miller (1986) scheme (Janjic 1994), resolvable-scale condensation, explicit cloud water/ice prediction, and short- and longwave radiation, are incorporated in both models. The resolvable-scale condensation is invoked for relative humidity (RH) greater than saturation relative humidity (SATRH), where SATRH is prescribed to be 0.75 for land points and 0.90 for the over the water points. For RH values greater than SATRH, a fraction of (RH − SATRH) q_s is condensed and the remaining part is used to increase the RH. Here q_s is the saturation mixing ratio. Note that RH in the model can become 100% with this scheme. The above formulation of resolvable-scale condensation is documented in Zhao and Carr (1997).

The convective release of latent heat in upright columns is evaluated in the two models using the modified Betts–Miller scheme cited above. A parameterization procedure for slantwise convection is not employed. Strong upward motion and condensational heating in deep slanted columns often occur in both MESO and Eta forecasts. Horizontal and vertical structures in a few cases investigated are found to be similar to those expected in SWC (see sections 3–4). Resolvable-scale condensation is found to be much greater than the parameterized convective condensation in the SWC areas. The intensity of vertical motions and precipitation is generally greater in MESO than in Eta in the SWC areas. In a previous study the development of SWC in 38-layer versions of MESO and Eta in a 1993 blizzard case over the eastern United States was presented (Mathur and Baldwin 1995). A grid spacing of 40 (80) km was employed in MESO (Eta) in the above case; the intensities of vertical motion and precipitation in the SWC area were greater in MESO than in Eta. Thus, the impact

of increasing the horizontal resolution, and perhaps the vertical resolution, is significant in the SWC areas in NCEP's η coordinate–based models. The enhancement of vertical motion with an increase in the resolution is usual in hydrostatic models.

The postprocessed data on constant pressure (p-) surfaces (25-mb interval) from MESO are routinely available at a lower resolution of 40 km on a Lambert conformal grid. The procedure employed is described in Treadon (1993). The processed data were used in this study and the General Meteorological Package (desJardins et al. 1996, 1997) for plotting meteorological data was utilized for analyzing the data. The forecasts from MESO in a few copious precipitation events during 1996 were examined. Although, we have recorded the development of slantwise vertical motions in many cases, we present results from only one case here for the purpose of illustrating the SWC development in MESO. As noted above in this section, another example of SWC development in the η coordinate–based models was discussed in an earlier study (Mathur and Baldwin 1995).

Changes in model atmospheric structure during the evolution of SWC in the 24-h MESO forecast from 1500 UTC 1 February 1996 are discussed in the following sections. Widespread snow or rain occurred over the southeastern United States during the above forecast period, with observed equivalent liquid amounts of 2–5 cm along a weak frontal zone extending from central Louisiana to eastern North Carolina. Intense SWC developed along this front during the 9–18-h period in the MESO forecast. In the operational MESO run, the forecasts are routinely output at 3-h intervals except that the condensational heating rates are not saved. To study the vertical distribution of condensation heating rates in SWC columns, we integrated the current version (implemented operationally in February 1997) of the model for this study and stored condensational heating rates during the forecast. Also, the forecast data were saved at 1-h intervals during the above-cited SWC period in this integration. The current 1997 operational version of MESO uses more advanced physical parameterization procedures than the 1996 operational version. The structure of SWC in both versions was, however, similar.

The distribution of vertical velocity in pressure coordinates (ω) at 500 mb in the SWC area is discussed in section 3; it is shown that the maximum upward motion in a propagating updraft over the southeastern United States increases between 9 and 13 h (times given refer to the number of hours into the forecast), and thereafter it decreases. In section 4 we present cross sections of various fields along a line that passes through the middle tropospheric maximum upward motion point and is perpendicular to the mean tropospheric thermal wind between 850 and 300 mb (westerly over the maximum in ω discussed here). The cross sections at 10, 12, 13, and 15 h are shown to capture the time evolution of SWC, cross sections of geostrophic pseudoangular
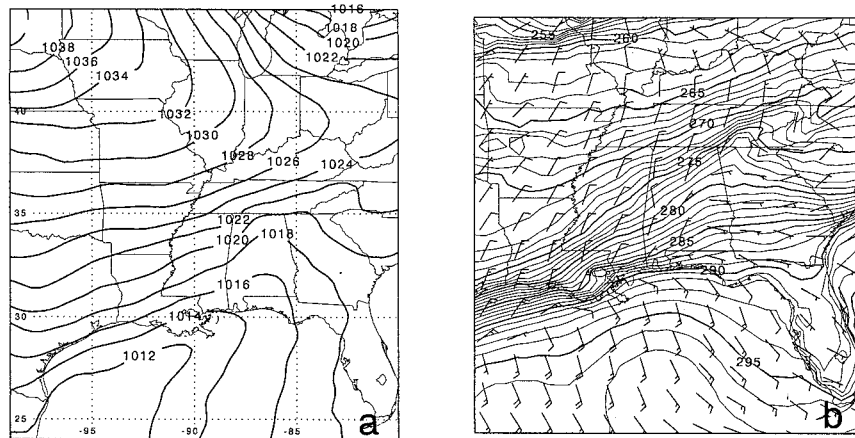
FIG. 1. Forecast surface fields at 13 h: (a) mean sea level pressure (2-mb intervals), (b) winds (half-barb = 2.5 m s^{-1}) at 10-m level above the ground, and temperature (1 K intervals) at 2-m level above the ground.

momentum M_g and the equivalent potential temperature θ_e are discussed first. Here M_g is defined as

$$M_g = fs - u_{gn},$$

where the normal component of the geostrophic wind u_{gn} is taken as positive if it blows out of the plane of the cross section, s is the horizontal distance from the origin of the cross section, and f is the Coriolis parameter.

The vertical structure of moist potential vorticity is examined to further ascertain whether the conditions favorable for CSI developed during the integration. MPV is defined as

$$\text{MPV} = -g\left(\zeta_a \frac{\partial \theta_e}{\partial p} - \frac{\partial \theta_e}{\partial x}\frac{\partial v}{\partial p} + \frac{\partial \theta_e}{\partial y}\frac{\partial u}{\partial p}\right),$$

where ζ_a is the absolute vorticity, (u, v) the horizontal components of the wind, and g is the acceleration due to gravity.

3. Horizontal structure in the frontal area

During the forecast period discussed in this paper widespread snow or rain was reported along a cold front (hereafter referred to as front C) that extended from southern Louisiana to western Virginia. Significant rainfall amounts were also observed along the Gulf Coast in association with a stationary front (hereafter referred to as front S) described below. The forecast frontal structure and a comparison of observed and forecast precipitation are now presented.

a. Surface features

It was noted in section 2 that the maximum vertical motion at 500 mb developed over the southeastern United at 13 h. The forecast mean sea level pressure

at 13 h indicates an inverted trough extending from the northwestern Gulf of Mexico to Virginia (Fig. 1a). This trough was nearly stationary during the 9–18-h SWC forecast period cited in section 2, and was most pronounced at 13 h. The winds at 10 m, and the temperature at 2 m, above the model ground level at 13 h (Fig. 1b) indicate the locations of the frontal zones. Frontogenesis occurred in the area extending from southern Louisiana to western Virginia, and a broad zone of enhanced temperature gradient developed by 13 h (the cold front "C" cited above). In this regard notice that northerlies prevail to the north of the front C, whereas winds are mostly from the east to the east of the front C (Fig. 1). The SWC area formed on the cool side of the front C, in northern Louisiana. Despite the weak winds, the potential temperature gradients increased a little in the front C area during the SWC period, and these were of the order of 6–8 K (100 km)$^{-1}$ at low levels in some parts of the front C, with weaker gradients in the surrounding areas. A zone of high temperature gradient extended from the western Gulf of Mexico eastward to the Florida panhandle (the stationary front "S" cited above). Front S was initially a cold front that moved over the northern Gulf of Mexico. Southerlies strengthened to the south of this front during 10–13 h, and this front remained nearly stationary during the next several hours.

b. Vertical motion

The distribution of ω between 10 and 15 h at 500 mb is shown in Fig. 2. A maximum in upward motion develops by 10 h over Louisiana with maximum upward velocity (-25×10^{-3} mb s^{-1}) between 700 and 500 mb. This maximum upward motion area is displaced toward the east with time, and the maximum upward velocity occurs at 13 h at 500 mb. The minimum in ω at this hour is -24×10^{-3} mb s^{-1} at 700 mb, $-46 \times$
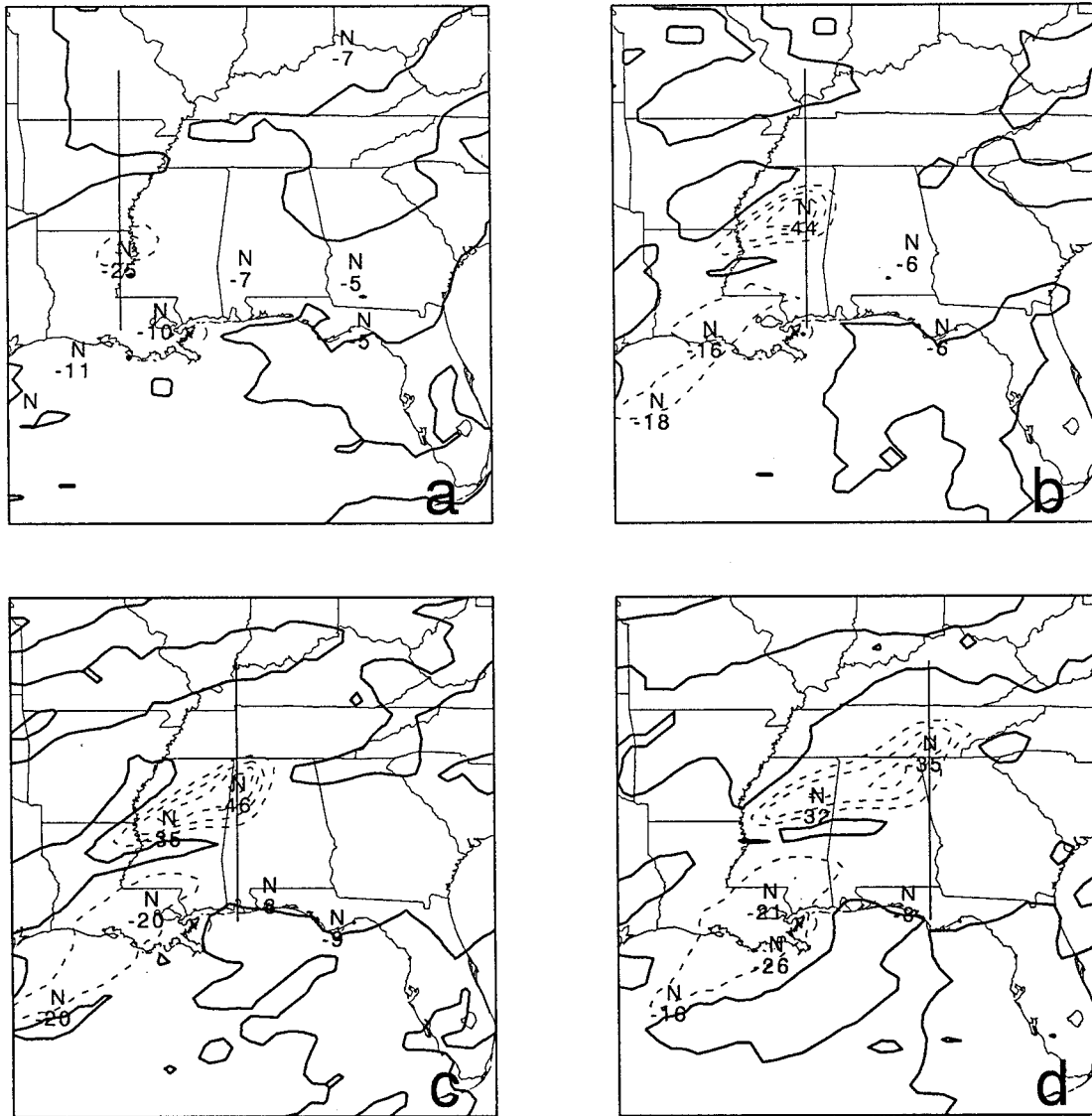
FIG. 2. Forecast vertical motion (dashed, 10×10^{-3} mb s^{-1} intervals; zero line solid) at 500 mb: (a) 10 h, (b) 12 h, (c) 13 h, and (d) 15 h. North–south solid line segments show cross section locations. Local minima of ω (maxima of upward velocity) indicated by N.

10^{-3} mb s^{-1} at 500 mb, and -33×10^{-3} mb s^{-1} at 350 mb. After 13 h, the maximum upward velocity decreases as it is displaced farther to the east (Fig. 2d). We will refer to this translating maximum of upward motion as cell A in the following.

The circulation in the above-cited updraft region satisfies the criteria for CSI listed in section 1. Notice that as cell A intensifies, the upward vertical motion area elongates toward the west-southwest and additional maxima develop. [In this elongated upward motion area two maxima develop at 500 mb (Fig. 2), and 3 (5) centers develop by 15 (17) h at 700 mb (not shown).] We will refer to this elongated area of upward motion as the ω band, or simply band, in the following. The

development of multiple mesoscale updrafts under CSI conditions has been documented in the observational case study of Seltzer et al. (1985, their Fig. 1 shows variation in radar echo intensity along the updraft), and in numerical studies (e.g., Lindstrom and Nordeng 1992, their Fig. 7a). Development of relatively narrow updrafts is consistent with the theory of Xu (1986) (criteria 4). Mean thermal winds between 850 and 300 mb around this elongated upward motion area are mostly from the west to west-southwest with relatively little variation in the direction of the thermal wind; the axis of the elongated upward motion area is nearly aligned with the mean thermal wind (this satisfies criteria 1 and 3). In section 4a it will be shown that an area of negative MPV

exists in the vicinity of the band (criteria 2). Note also that the band translates with the mean flow, which satisfies criteria 5 for CSI. It should be noted that the development of such precipitation bands has been attributed in previous studies to either symmetric instability (Bennetts and Hoskins 1979; Emanuel 1979) or frontogenesis (Bjerknes 1919; Sawyer 1956; Eliassen 1959; Hoskins and Bretherton 1972; Ley and Peltier 1978). The contribution of these two dynamical processes in the development of strong upward motion will be discussed in sections 4–5. It will be evident that the band develops due to release of CSI and the resultant circulation induces weak frontogenesis (criteria 6).

c. Precipitation

Observed and predicted precipitation amounts accumulated over the 24-h period ending at 1500 UTC 2 February 1996 are shown in Fig. 3. The river forecast center network of observations and radar data were used for producing the analysis shown in Fig. 3a. These data have been routinely employed for some time at NCEP to obtain the observed rainfall analysis (M. Baldwin 1997, personal communication).

Observed (liquid equivalent) amounts of 2–5 cm occurred along front C, and 2–3-cm maximum amounts occurred near the coastal Gulf of Mexico area (Fig. 3a). The forecast total precipitation amounts in the front C area are somewhat larger than the observed, and the model overpredicts the rainfall amounts over the Gulf Coast area (Fig. 3b). Notice that the precipitation over the Gulf Coast is associated with both parameterized convective and resolvable-scale condensation, whereas the precipitation in the front C area is mainly due to the resolvable-scale condensation (Figs. 3c–d).

d. Upper-tropospheric flow

The maximum divergence at 350 mb during the period 10–15 h (Fig. 4) is located close to the 500-mb maximum upward motion area (Fig. 2). The maximum divergence at 350 mb increases considerably between 10 h (8×10^{-5} s^{-1}) and 13 h (24×10^{-5} s^{-1}). Recall that the 500-mb upward motion also increased during the above period (section 3b). The level of maximum divergence rises as the upward motion increases; the maximum divergence occurs at 450 mb at 10 h and near 300 mb after 12 h. The lifting of the level of maximum divergence is caused by the warming in the band area, especially in the middle troposphere, that arises due to the upward transport of sensible and latent heat in the band (see section 6a). Notice that from 13 to 15 h both the 350-mb maximum divergence (Figs. 4c–d) and 500-mb maximum upward motion (Figs. 2c–d) values have decreased.

Southwesterly winds prevail over the maximum divergence area at 350 mb during the 10–15-h period (Fig. 4). A wind minimum (<40 m s^{-1}) develops in the maximum divergence area during the period 10–12 h (Fig. 4), above the region of midtropospheric upward motion. Notice also that the upward motion, weaker than at 500 mb (Fig. 2), occurs in the band area at 350 mb (Fig. 5). The size of the wind minimum area increases considerably by 15 h (Fig. 4d) and it grows further during 15–18 h (not shown). Notice also that a minimum wind speed (<30 m s^{-1}) area develops near the Louisiana coast during 10–15 h. The development of the wind minima in the upper levels of the ω bands is due to vertical momentum transport, and its evolution is discussed further in section 4.

An area with negative absolute vorticity (AV) appears just to the north (on the baroclinically cool side) of the band area at 12 h (Fig. 5b); the negative AV area becomes elongated and the maximum negative AV values move farther to the north of the band area during 12–15 h. The development of upper-level negative AV anomalies on the baroclinically cool side of updrafts has also been simulated in numerical studies of dry symmetric instability (Thorpe and Rotunno 1989) and SWC (Lindstrom and Nordeng 1992; Seman 1994). Notice that the 350-mb winds (Fig. 4) in an area to the north of the negative AV area (Fig. 5) have increased by about 5 m s^{-1} during the 10–13-h period. Previous studies have shown that negative AV at the outflow level causes an increase in the mesoscale outflow winds in the negative AV region (Seman 1994; Blanchard et al. 1998) (see also section 4b).

Scattered areas with negative MPV occur at 350 mb during the entire integration period. A large negative MPV area extends southwestward from just south of the ω band at 10 h (Fig. 4a). An area with negative MPV develops over the maximum vertical motion area of the band by 12 h (Fig. 4b), and it covers most of the band area by 15 h (Fig. 4d). Horizontal and vertical advections of MPV between 10 and 15 h at 350 mb were computed; the increase in the maximum negative MPV value during 10–15 h was somewhat larger than that implied by these two terms. Processes that might have generated negative MPV were not investigated.

4. Slantwise vertical motions

Cross sections are presented to show the time evolution of various fields during the development of slanted vertical motion structure. As noted in section 2, the cross sections are drawn along a line that passes close to the 500-mb maximum upward motion point and is perpendicular to the thermal winds. Recall that the maximum vertical motion area is displaced eastward in time (Fig. 2), and therefore the location of the cross sections presented below shifts to the east with time. Note that for the south to north cross sections presented, $M_g = fy - u_g$, where y is the horizontal distance from the origin of the cross sections and u_g is the westward component of the geostrophic wind.
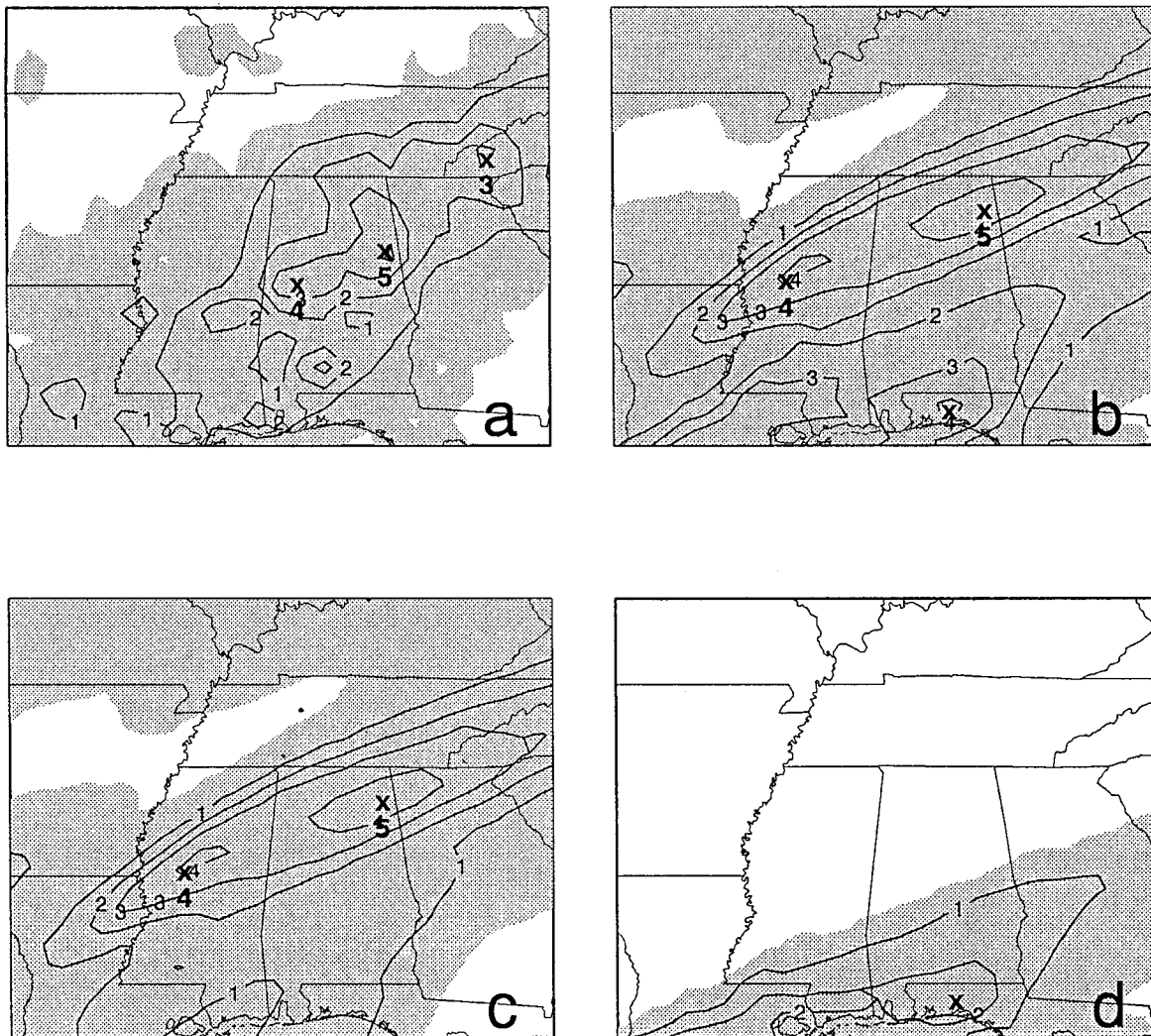
FIG. 3. Accumulated 24-h precipitation amounts (1-cm intervals) at 1500 UTC 2 February 1996: (a) observed, (b) forecast total, (c) forecast (resolvable scale), and (d) forecast (convective scale). Areas with amounts greater than 0.1 cm are shaded. Local maxima indicated by X.

a. Conditional symmetric instability

A necessary condition for CSI to occur in a saturated baroclinic atmosphere is that the slope of θ_e surfaces be greater than that of the M_g surfaces (Bennetts and Hoskins 1979; Emanuel 1983a). This is equivalent to requiring negative moist potential vorticity for CSI to occur (Bennetts and Hoskins 1979). The above theory assumes that the basic-state flow is two-dimensional, frictionless, and in thermal wind balance, and diabatic effects other than that due to condensation are neglected (Bennetts and Hoskins 1979; Emanuel 1983a).

The equivalent potential temperature θ_e in this study is computed using Eq. (38) in Bolton (1980); the formation of ice at subfreezing temperatures is not included in this diagnostic calculation. If the ice phase was included, then the diagnosed equivalent potential temperature θ_{ei} would be greater than θ_e at all points with nonzero specific humidity. The temperature and specific humidity along θ_e and θ_{ei} profiles through a saturated point (base of the profiles) would be the same below the freezing level. Above the freezing level the temperature (specific humidity) would be higher (lower) for the θ_{ei} than for the θ_e profile. Because the formation of ice during resolvable-scale condensation is included in MESO but is not included in the diagnostic evaluation of θ_e, the difference in the θ_{ei} and θ_e profiles should be taken into account when interpreting MESO forecasts. Consider a case where θ_e is the same between two levels L1 and L2 above the freezing point, and L1 is the lower level. (As an example, see the 320 K θ_e contour in Fig. 6b between 600 and 500 mb; the freezing level was located near 700 mb.) Note that θ_{ei} will be greater at L1 than at L2. Therefore, a neutral profile (θ_e constant in vertical) above the freezing level may be conditionally unstable because of formation of ice during a MESO forecast. Thus, the areal extent of the conditionally un-
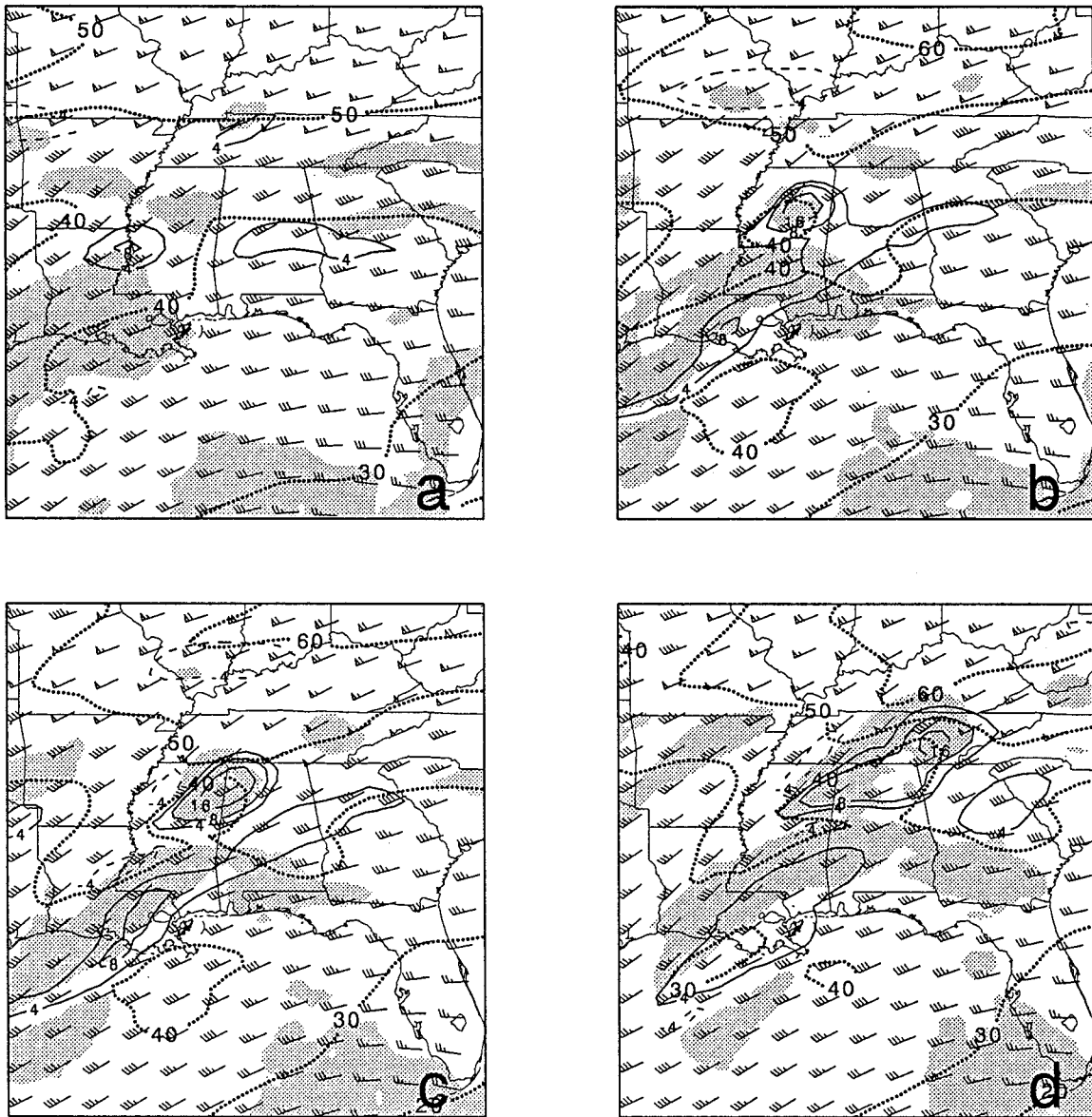
Fig. 4. Forecast winds (half-barb = 5 m s^{-1}) and isotachs (thick dotted, 10 m s^{-1} intervals), areas with negative moist potential vorticity (shaded), divergence and convergence (solid and dashed, respectively; -4, 4, 8, 16 $\times$ 10^{-5} s^{-1} contours) at 350 mb: (a) 10 h, (b) 12 h, (c) 13 h, and (d) 15 h.

stable region above the freezing level discussed later in this section may be larger than that implied by area with $\partial\theta_e/\partial p > 0$.

The distribution of equivalent potential temperature in MESO might be also controlled by the saturation criteria (less than 100%, SATRH $<$ 1, see section 2) used for invoking resolvable scale condensation. Thermodynamic considerations show that when the resolvable-scale condensation is evaluated at RH less than 100%, then the lapse rate in the conditionally unstable regions is adjusted toward a rate steeper than the pseudoadiabatic (Mathur 1983). This effect will tend to pro-

duce an equivalent potential temperature that is lower than that would be obtained using 100% saturation criteria for resolvable-scale condensation. Recall that only a fraction of excess moisture [$>$(SATRH) q_s] is condensed in MESO, so that the RH, at a later time, can approach 100% (section 2). Therefore, the impact of using SATRH $<$ 1 in MESO will not be as large as would be expected if all excess moisture is condensed [condition postulated in Mathur (1983)].

South to north cross sections of θ_e and M_g at 10 h show the development of the slanted vertical motions in the lower troposphere near 32°N (Fig. 6a). Close
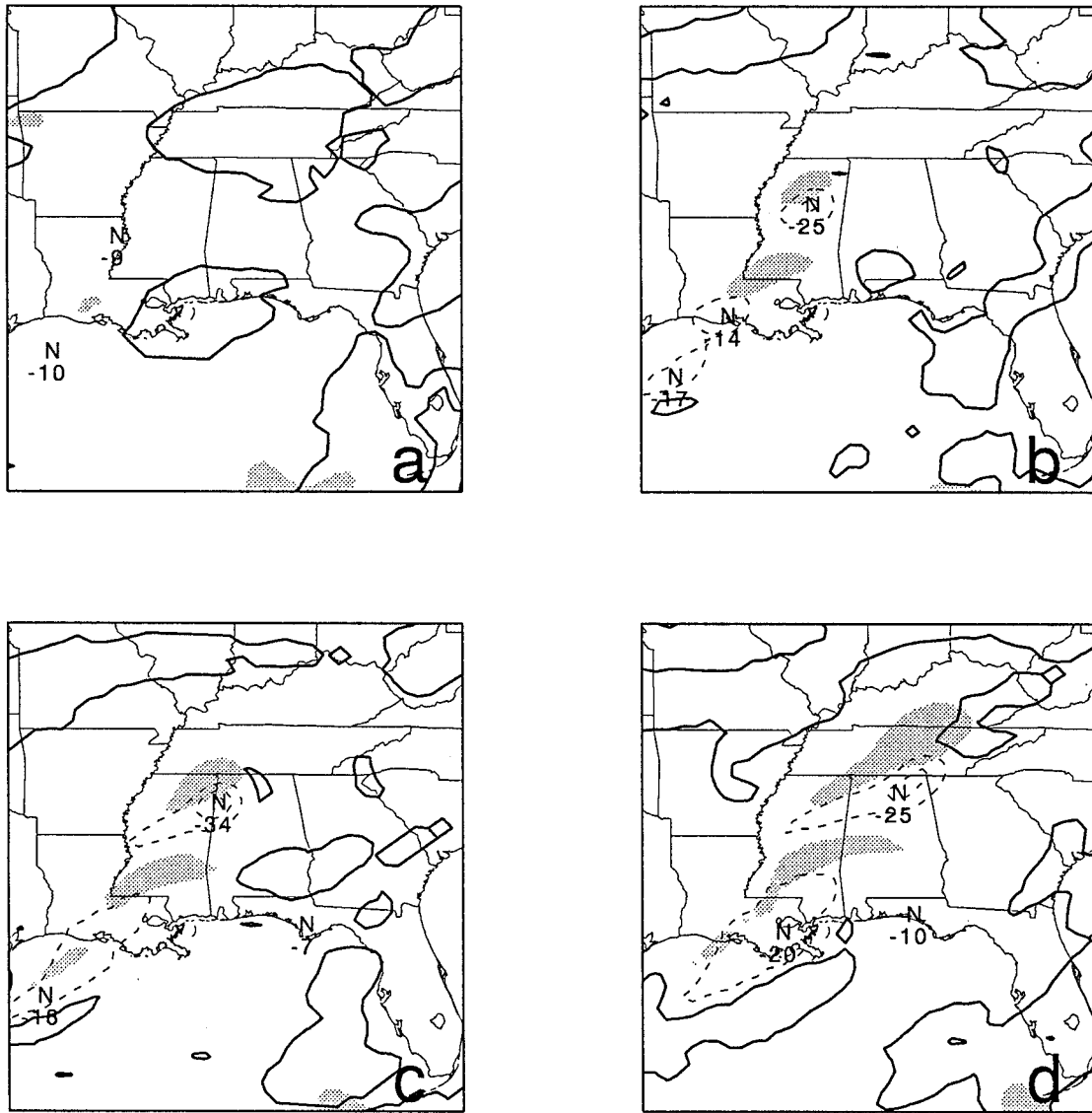
FIG. 5. Forecast vertical motion (0 solid, negative dashed, 10×10^{-3} mb s^{-1} intervals, local minima indicated by N) and negative absolute vorticity areas (shaded) at 350 mb: (a) 10 h, (b) 12 h, (c) 13 h, and (d) 15 h.

inspection of the relative orientation of the θ_e and M_g surfaces in Fig. 6a reveals that the θ_e surfaces are slightly more vertical than the M_g surfaces in the lowest 100–200 mb of the atmosphere; a potential for CSI therefore exists in this region (criteria 2 of section 1). The CSI is realized because the RH is greater than 90% and significant resolvable-scale condensation (latent heat release) takes place in the area (Fig. 7a). As shown by Bennetts and Hoskins (1979) and Emanuel (1983a), a CSI updraft will be oriented along the surfaces of neutral buoyancy. In our case of widespread saturation, these surfaces will coincide with θ_e surfaces. Note that a slantwise updraft develops approximately along the θ_e surfaces between 10 and 13 h (Figs. 6a–c) in the region where CSI conditions exist, and by 13 h the

circulation vectors (flow in the plane of the cross section) below 400 mb become nearly aligned with the θ_e = 320 K contour that lies nearly along the axis of slantwise vertical motions. Notice also that at 10 h, stable ($\partial \theta_e / \partial p < 0$) conditions (to upright convection) prevail on the cool side of the axis of cell A below 600 mb (Fig. 6a).

In the region of maximum upward motion in the middle troposphere, conditionally unstable conditions ($\partial \theta_e / \partial p > 0$) exist (Fig. 6a), and nearly upright vertical motions have developed. Resolvable-scale condensation with maximum heating rate of 3 K h^{-1} occurs in the upright vertical motion region (Fig. 7a). This may be considered an example of development of grid-scale convection. Previous studies (e.g., Molinari and Dudek
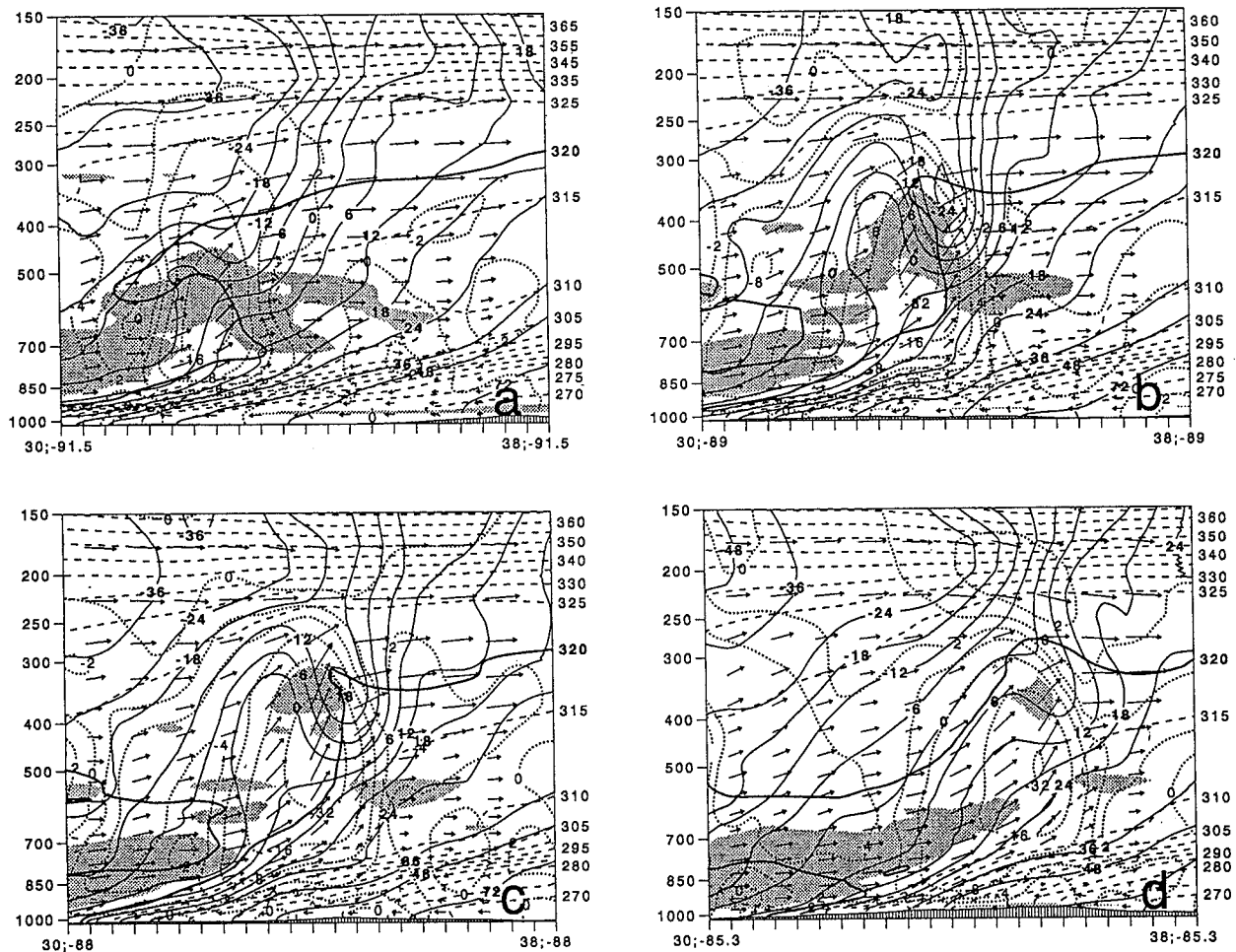
FIG. 6. Cross sections through the maximum vertical motion areas. Ordinate is pressure (mb); abcissa is lat–long. Geostrophic pseudoangular momentum M_g, (solid, -48, -36, -24, -18, -12, -6, 0, 6, 12, 18, 24, 36, 48, 72 m s^{-1} contours), equivalent potential temperature (dashed, 5 K intervals, except 320 K, which is thick solid), and vertical motion (dotted, -32, -16, -8, -4, -2, 0, 2×10^{-3} mb s^{-1} contours): (a) 10 h, (b) 12 h, (c) 13 h, and (d) 15 h. Areas with $(\partial\theta_e/\partial p) > 0$ are shaded. Circulation vectors (thinned) are also shown.

1992) have suggested that grid-scale forcing may saturate vertical columns in a fine mesh model, and grid-scale convection may become dominant and determine the vertical distribution of condensational heating in such columns.

Note that the negative values of MPV exist over nearly the entire upward motion region of cell A below 450 mb at 10 h (Fig. 8a). A comparison of Figs. 6a–b and 8a–b shows that between 10–12 h the level of maximum upward motion has shifted upward, and the conditionally unstable region with negative MPV in the midtropospheric region of cell A has also moved upward. The upper portion of this negative MPV area becomes connected with the negative MPV area that is located between 30° and 32°N. [The negative MPV areas to the south of the updraft and over the updraft are not connected at 350 mb (Fig. 4b), but as can be seen from Fig. 8b these two negative areas are connected at the 325–300-mb levels.] Stable conditions $(\partial\theta_e/\partial p < 0)$ ex-

ist in the above-cited negative MPV region between 400 and 300 mb at 12 h; note that the vertical motion contours slant southward toward the above-cited upper-tropospheric negative MPV area (Fig. 6b).

With the lifting of the level of maximum vertical motion, the depth of slantwise vertical motions has increased in the lower part of the troposphere (cf. Figs. 6a–b), and the level of maximum heating has also shifted upward (cf. Figs. 7a–b). Also, the heating rates of 1–3 K h^{-1} occur over a wider area at 12 h than at 10 h. Note also that θ_e in the middle troposphere in the southern part of the updraft has also increased during the above period and a nearly moist adiabatic lapse rate has developed in the updraft area between 700 and 350 mb (see the $\theta_e = 320$ K contour in Fig. 6b). Note that at 13 h the $\theta_e = 320$ K contour below 700 mb lies nearly along an M_g surface that nearly coincides with the axis of slanted upward motions (Fig. 6c). The evolution of θ_e and M_g surfaces between 10 and 15 h is
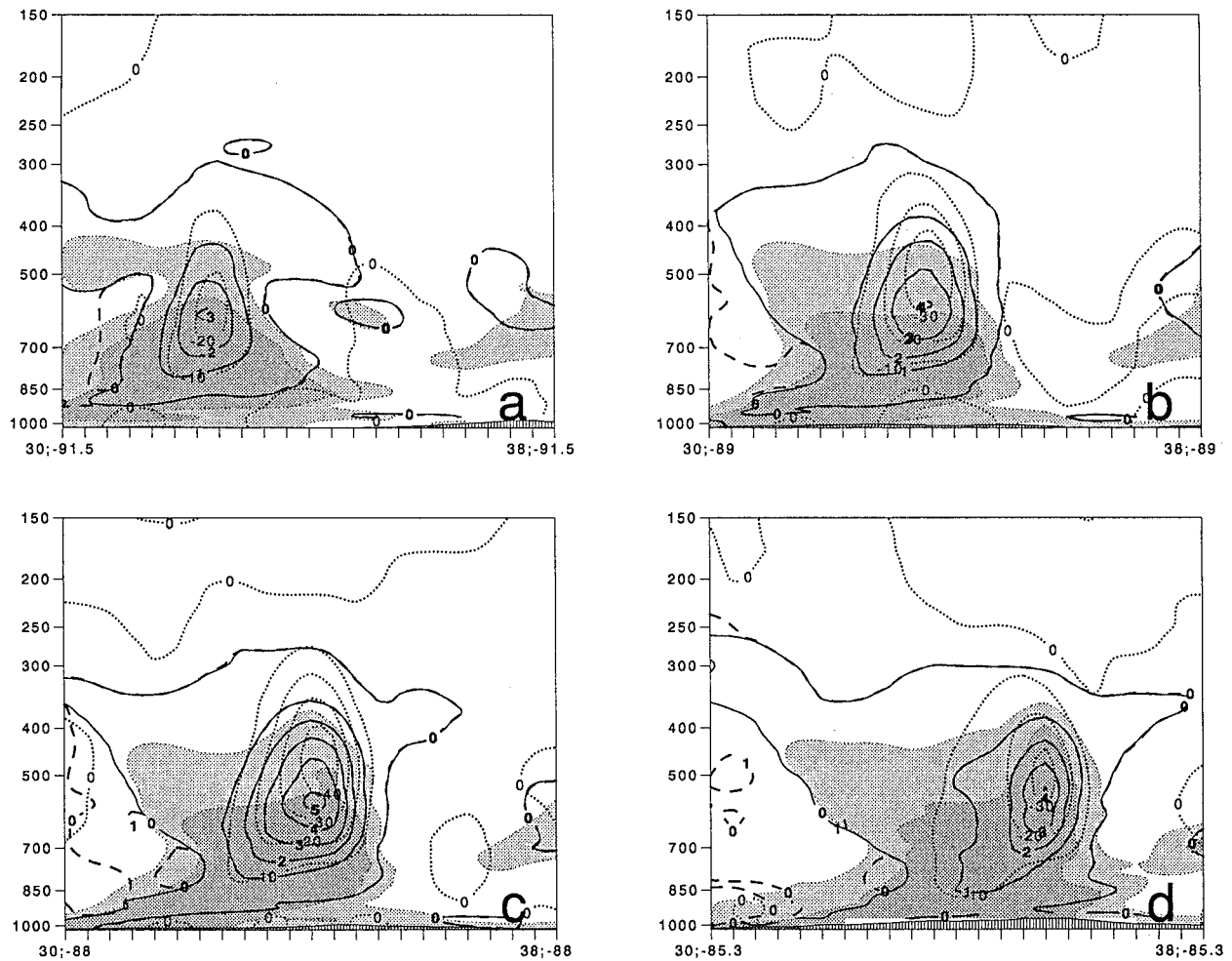
FIG. 7. Cross sections through the maximum vertical motion areas. Total and resolvable-scale condensational heating rates (dashed and solid, respectively, 1 K h^{-1} intervals) and vertical motion (dotted, 10×10^{-3} mb s^{-1} intervals): (a) 10 h, (b) 12 h, (c) 13 h, and (d) 15 h. Areas with RH exceeding 80% (lightly shaded) and 90% (heavily shaded) are also shown.

similar to that expected during the release of CSI or slantwise convective adjustment [Seltzer et al. 1985; Wolfsberg et al. 1986; Persson and Warner 1991 (Fig. 7d)].

Previous studies using idealized initial data (Thorpe and Rotunno 1989) and synoptic initial state (Lindstrom and Nordeng 1992) have shown that the buckling of absolute momentum (M) surfaces occurs in the release of the symmetric instability. In the above studies actual winds were used for evaluating M (geostrophic winds are used in evaluating M_g). Lindstrom and Nordeng integrated a primitive equation model with and without the inclusion of a parameterization procedure for SWC. Significant buckling of M surfaces developed only in the integration in which SWC parameterization procedure was included. Recall that an SWC parameterization scheme is not used in MESO (section 2). Strong buckling in M_g (Figs. 6b–d), but only a weak buckling in M surfaces (not shown), develops above 500 mb in the cell

A area in our study. This difference in structure between M and M_g is related to the development of strong ageostrophic winds; it will be shown in section 4b that the ageostrophic AV and geostrophic AV have opposite signs over most of the updraft area.

b. Absolute vorticity

Development of negative AV at 350 mb was discussed in section 3d (Fig. 5). Heavy lines in Fig. 8 enclose the areas with negative AV. It is evident that negative AV develops in a deep layer in the upper troposphere on the baroclinically cool side of cell A. This AV structure is what one would expect from vortex-line tilting by a relatively narrow and intense updraft in a baroclinic atmosphere (for another example, see Seman 1994).

A comparison of Figs. 6 and 8 shows that the 0 (-8) AV contour at 12 (13) h lies just north of the cusplike feature in the $\theta_e = 320$ K contour, and also just north
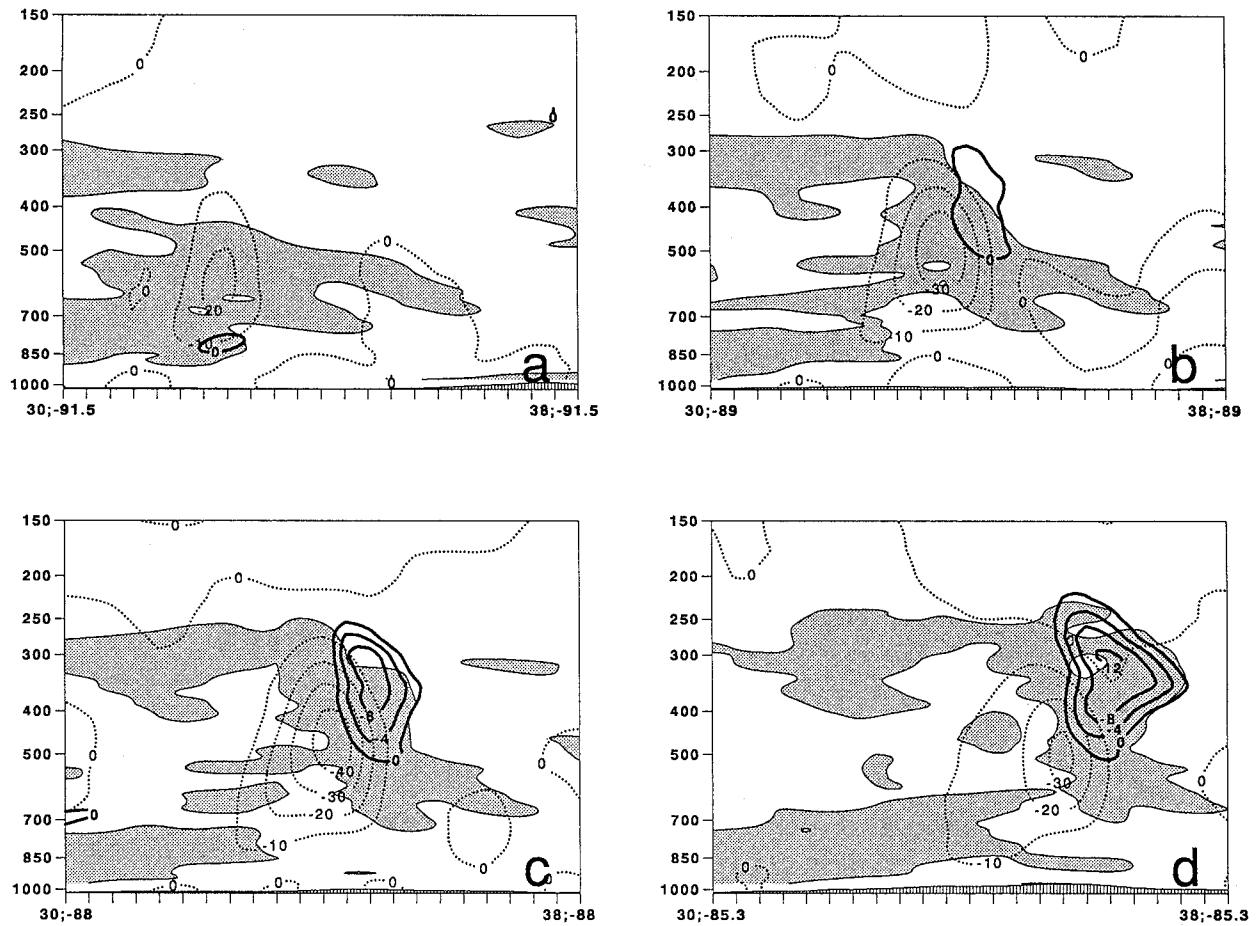
FIG. 8. Cross sections through the maximum vertical motion areas. Vertical motion (dotted, 10×10^{-3} mb s^{-1} intervals), areas with negative moist potential vorticity (shaded), and negative absolute vorticity (thick solid, 4×10^{-5} s^{-1} intervals): (a) 10 h, (b) 12 h, (c) 13 h, and (d) 15 h.

of the local minimum in the M_g field. For two-dimensional flows, $\zeta_{ga} = \partial M_g/\partial y$ implies that ζ_{ga} will be negative to the south side of this local minimum in M_g and positive to its north (Fig. 9a). Here ζ_{ga} is the geostrophic AV and y is the distance from south to north. Ageostrophic winds have a large rotational component; large negative values of ageostrophic AV develop to the north side of this local minimum in M_g field (Fig. 9b). The geostrophic AV and ageostrophic AV have opposite signs over large areas, and the net AV has a dipolelike structure in the middle and upper troposphere with the positive values on the warm side and negative values on the cool side of the updraft (Fig. 9c). The upper-level net AV distribution simulated here has also been simulated in other numerical models of SWC (Seman 1991; Lindstrom and Nordeng 1992; Seman 1994).

As noted in section 3d, the mesoscale outflow winds increased by about 5 m s^{-1} through the negative AV area. Release of inertial instability in the negative AV accelerates the outflow (Seman 1994; Blanchard et al. 1998). This enhanced outflow, in turn, has been shown

to promote further lifting in the area of the latent heating, reinforcing the convection and assisting in the development of new convection (Seman 1994; Blanchard et al. 1998). In this regard note the upper-level divergence is centered close to the southernmost edge of the AV < 0 region (Figs. 8 and 10), and develops a slanted pattern. The slanted axis of divergence (convergence) lies above (below) the slanted axis of vertical motion (Fig. 10). The levels of maximum vertical motion, convergence, and divergence are displaced upward during the period of intensification (10–13 h).

c. Winds

Gradients in diabatic heating rates (Fig. 7c) and upward motion (Fig. 6c) at 13 h in the middle troposphere are stronger to the north than to the south of the maximum upward motion axis. Mainly because of differential heating, potential temperature gradients increase in a deep column (500–300 mb) between 10 and 13 h to the north side of cell A (not shown). Consequently
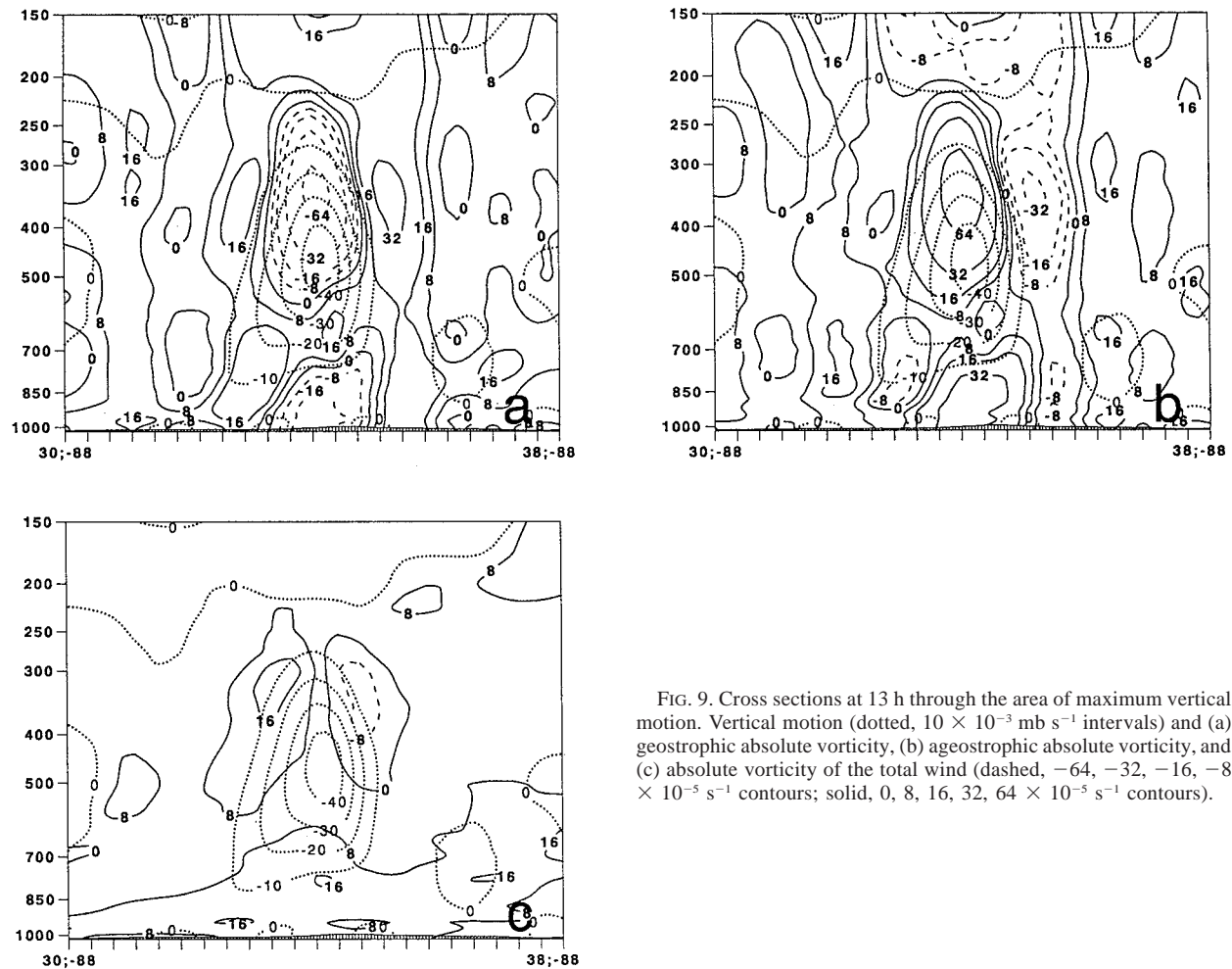
FIG. 9. Cross sections at 13 h through the area of maximum vertical motion. Vertical motion (dotted, 10×10^{-3} mb s^{-1} intervals) and (a) geostrophic absolute vorticity, (b) ageostrophic absolute vorticity, and (c) absolute vorticity of the total wind (dashed, -64, -32, -16, -8 $\times 10^{-5}$ s^{-1} contours; solid, 0, 8, 16, 32, 64 $\times 10^{-5}$ s^{-1} contours).

large pressure gradients develop in the middle and upper troposphere to the north side of the updraft. Strong geostrophic winds in the middle and upper troposphere are therefore predicted to the north side of the updraft (Fig. 11b). In contrast, the potential temperature gradients decrease somewhat on the south side of the updraft in most of the 500–300-mb column between 10 and 13 h; consequently, weaker geostrophic winds develop on the south side of the vertical motion axis (Fig. 11b). Note that the geostrophic winds have a mostly westerly component, and the above-cited distribution of wind speeds implies that the geostrophic vorticity will be negative at upper levels in cell A and it will be positive to the north of cell A. This distribution of relative vorticity gives rise to the geostrophic AV distribution shown in Fig. 9a.

Winds above 800 mb are from the west in the band area, and westerlies increase with height (Fig. 11a). Strong upward transport of low-level momentum occurs in cell A and the band region (Fig. 12). The development of subgeostrophic winds over a large depth of the updraft above 500 mb is probably mainly due to this up-

ward flux of low momentum air from the low levels (Newton 1950; Seman 1994), whereas the development of the geostrophic wind structure is associated with the diabatic heating mechanism cited above.

For an inviscid atmosphere, dv/dt is proportional to $-u_{ag}$, and also to the difference $M - M_g$. Here u_{ag} is the westerly component of the ageostrophic wind. Notice that the ageostrophic easterly component ($u_{ag} < 0$) is large to the north side of the updraft between 300 and 500 mb (Fig. 11c). Therefore in this region the wind is being accelerated strongly to the north, and M and M_g surfaces are not expected to lie close to each other. As noted in section 4a, the pronounced buckling that develops in M_g surfaces in this region does not appear in M surfaces.

5. Frontogenesis

The intensity of a front is often specified by the magnitude of the maximum horizontal potential temperature gradient, and its change in intensity by the frontogenetical function $(d/dt)|\nabla_p \theta|$. Here, $\nabla_p \theta$ is the potential
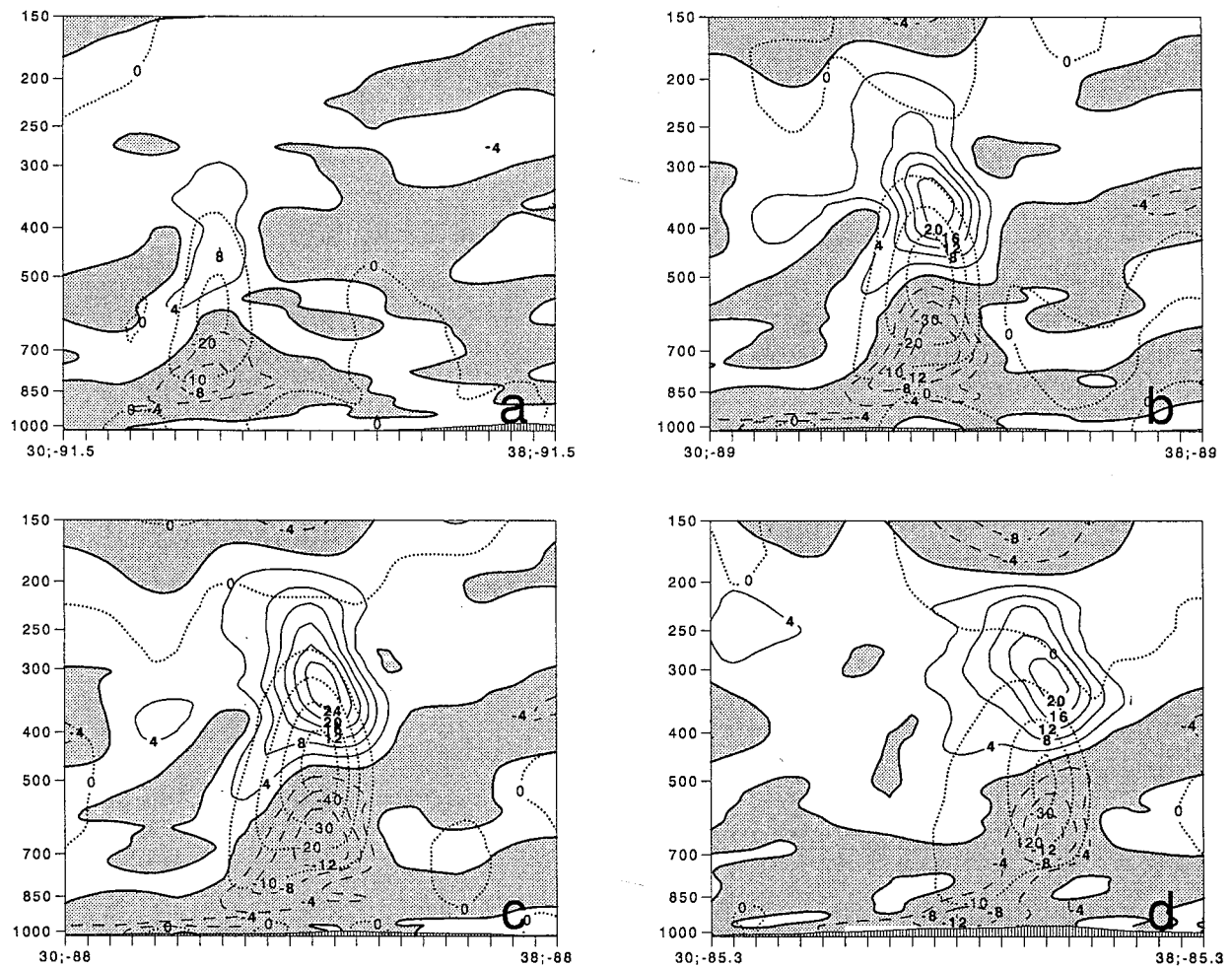
FIG. 10. Cross sections through the maximum vertical motion areas. Vertical motion (dotted, 10×10^{-3} mb s^{-1} intervals), divergence and convergence (solid, dashed and shaded, respectively; 4×10^{-5} s^{-1} intervals): (a) 10 h, (b) 12 h, (c) 13 h, and (d) 15 h.

temperature gradient on a constant pressure surface, and d/dt is the Lagrangian time derivative. A more general expression for the frontogenetical function (time rate change of three-dimensional potential temperature gradient with height as the vertical coordinate) is derived in Miller (1948) and Bluestein (1986).

The time rate change of gradient of potential temperature in any direction (say y) on a pressure surface may be obtained from $(d/dt)(-\partial\theta/\partial y)$. It can be easily shown that

$$\frac{d}{dt}\left(-\frac{\partial\theta}{\partial y}\right) = \left(\frac{\partial u}{\partial y}\right)\left(\frac{\partial\theta}{\partial x}\right) + \left(\frac{\partial v}{\partial y}\right)\left(\frac{\partial\theta}{\partial y}\right) + \left(\frac{\partial\omega}{\partial y}\right)\left(\frac{\partial\theta}{\partial p}\right)$$
$$- \frac{\partial}{\partial y}\left(\frac{\partial\theta}{\partial t}\right).$$

Carlson (1991) takes the y direction to be perpendicular to the front, and provides physical interpretation of each term on the right-hand side of the above equation.

The first two terms are shear S and confluence C terms, respectively. The third is the tilting T term, and the fourth is the diabatic D term. Carlson points out that the maximum potential temperature gradient at every point along the front may not be in the direction perpendicular to the front.

Reed and Sanders (1953), and Haltiner and Martin (1957) proposed that, for convenience, the y axis be taken toward the lower potential temperature at each grid point so that the first term S vanishes. We have adopted this last definition of the y axis to investigate the role of frontogenesis in the development of slantwise motions discussed in section 4. The left-hand side of the above equation will be referred to as the frontogenetical function in the following.

The south to north cross sections for the frontogenetical function and its components C, T, and D at 10 and 13 h are shown in Figs. 13–14. In the formative stage of cell A (10 h), the slanted upward motions extend to about 700 mb. Frontogenetical forcing in this updraft
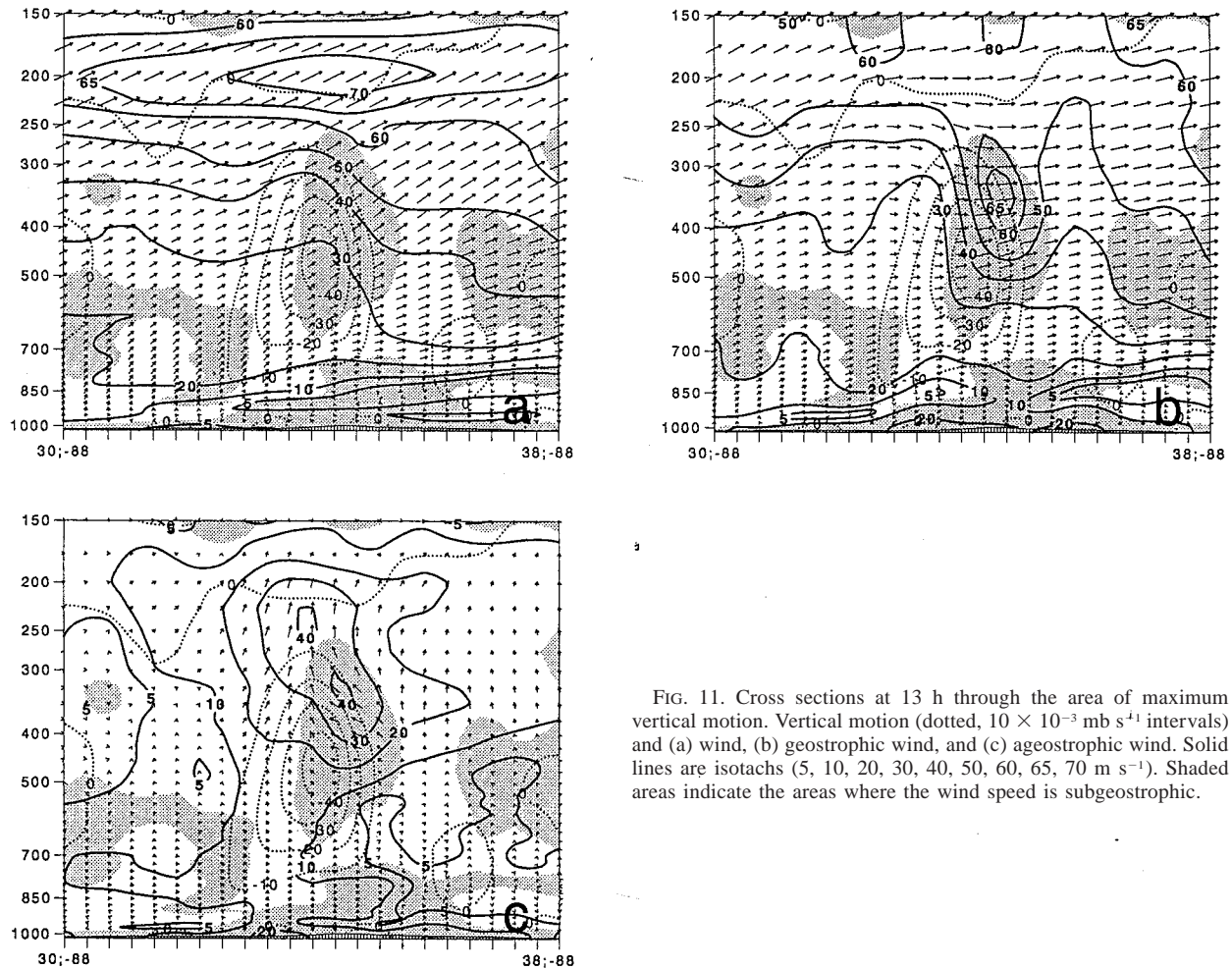
area is mainly due to the T term (Fig. 13), indicating that greater upward motion must be occurring on the cooler rather than on the warmer side (effectively an indirect circulation). In this regard, note that the ascending motion is stronger on the cold side (north) than on the warm side in the updraft area. In a shallow layer near 600 mb in the updraft, the D and C terms are frontogenetical and the T term is frontolytical. In the northern part of the midtropospheric updraft area both the T and D terms are strong but possess opposite signs and nearly cancel each other. Strong frontogenesis is also indicated near 400 mb in the region where the ω contours slant toward the south; the T term is strongly frontogenetic and greater in magnitude than the D term which is frontolytical.

The structure of D (Fig. 13b) and T (Fig. 13c) is similar to that expected in a pseudoadiabatic atmosphere with westerly thermal wind and a vertical motion field that is linear in the west–east direction. In this case the y axis of cross sections shown would have south to north orientation. In a pseudoadiabatic atmosphere the cooling due to the vertical advection term

$(-\omega\partial\theta_c/\partial p)$ is balanced by the resolvable-scale heating that is associated with the supersaturation due to the vertical advection of moisture $(-\omega\partial q_c/\partial p)$ Mathur 1983). Here, θ_c and q_c are, respectively, potential temperature and saturated mixing ratio along a pseudoadiabat. Therefore we may write,

$$D = -\frac{\partial}{\partial y}\left(\omega\frac{\partial\theta_c}{\partial p}\right)$$

and

$$T = -D - \omega\frac{\partial}{\partial y}\left(\frac{\partial\theta_c}{\partial p}\right).$$

If the horizontal gradients of equivalent potential temperature are small, then D and T would be zero near the maximum in ω on a pressure surface and D and T would have opposite signs elsewhere. Notice that T is zero along the axis of maximum vertical motion except near 600 mb, and D and T have opposite signs in many parts of the upward motion area (Figs. 13b–c).
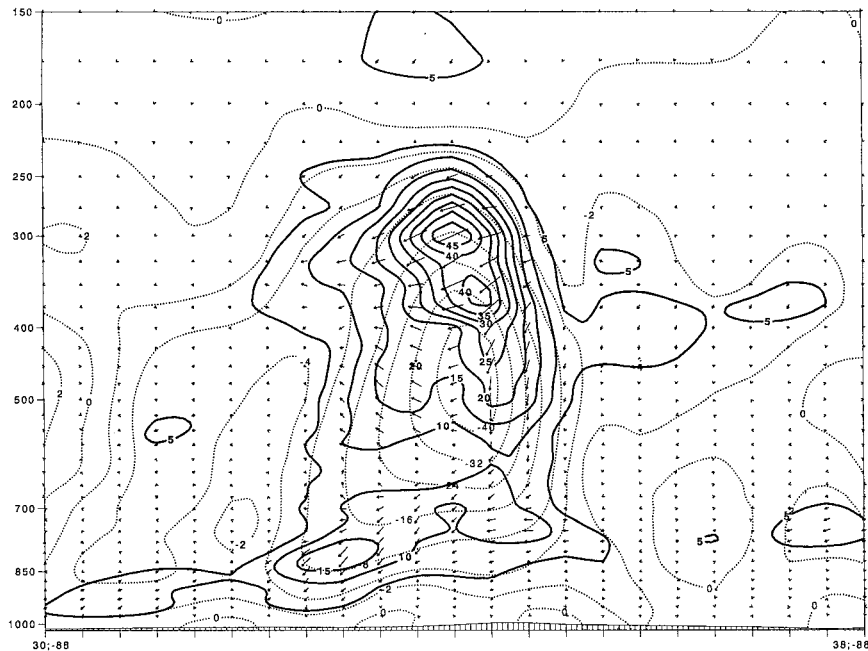
FIG. 12. Cross section of the wind tendency (5 m s^{-2} 3h^{-1} intervals) due to the vertical advection term through the area of maximum vertical motion (dotted, -40, -32, -24, -16, -8, -4, -2, 0, 2 $\times$ 10^{-3} mb s^{-1} contours) at 13 h.

Figure 14 shows that a strong frontogenetical (frontolytical) lobelike structure has developed in the $D(T)$ term on both the southern and northern sides of the maximum vertical motion area in the middle troposphere. It was noted in section 4b that the maximum upward motion in cell A develops in the middle troposphere at 13 h, and that slanted upward motions extend to higher levels at 13 h than at 10 h. All three terms $C, T,$ and D have greater magnitudes at 13 h (Fig. 14) than at 10 h (Fig. 13). Frontogenesis in the lower part of the slanted column at 13 h is mainly due to the T term, and in the upper portion to the D and C terms. Just to the north of the axis of maximum vertical motion around 300 mb, the C term has become strongly frontogenetical, and over parts of this area both D and T terms are also frontogenetic. Note also that the axis of total frontogenesis is displaced slightly to the baroclinically warm side of the updraft from the axis of maximum upward vertical motion (Fig. 14a). Emanuel (1983a) predicted a frontogenetical forcing by the SWC circulations on the baroclinically warm side of the SWC updraft.

Sanders and Bosart (1985) investigated the role of large-scale frontogenesis in a heavy snow storm case over the northeastern United States, using mainly rawinsonde data that were located about 250 km apart. They evaluated the geostrophic frontogenesis, and found it to be a maximum [about 1 K (100 km)$^{-1}$ (3 h)$^{-1}$] near the surface. Frontogenetical forcing terms are much greater in our case (by an order of magnitude); this may

be partly because our grid spacing is much smaller than that in the Sanders and Bosart (1985) study, and also because we are evaluating the mesoscale frontogenesis resulting from SWC in which the tilting and diabatic terms become very important. In many studies using observations, the tilting and diabatic terms are not evaluated because of a lack of sufficient information. All three terms at 13 h (Fig. 14) have similar magnitudes and do not cancel each other everywhere; this suggests that the diagnosis of frontogenesis in high-resolution models should include all terms.

Strong frontogenetical forcing develops at 13 h near 200 mb above the updraft area (Fig. 14a). The contribution to frontogenesis in this area is largely from the T term and to a smaller extent from the C term. The tilting term is strong despite weak (mainly downward) vertical motions because the vertical potential temperature gradients are large. If the subsidence is greater on the warmer side than on the cooler side then the T term will be frontogenetic. A similar example of frontogenesis in the middle troposphere in the region of subsidence was discussed by Reed and Sanders (1953). The potential temperature gradient at 200 mb over the updraft area increased from about 1 K (100 km)$^{-1}$ at 10 h to 6 K (100 km)$^{-1}$ at 14 h. Between 10 and 13 h, upward motion at 200 mb over the cell A area changes to downward motion (Fig. 6). Whether the above transformation and the development of high-level frontogenesis occurred due to the intensification of lower-level vertical motions, or the high-level frontogenesis played
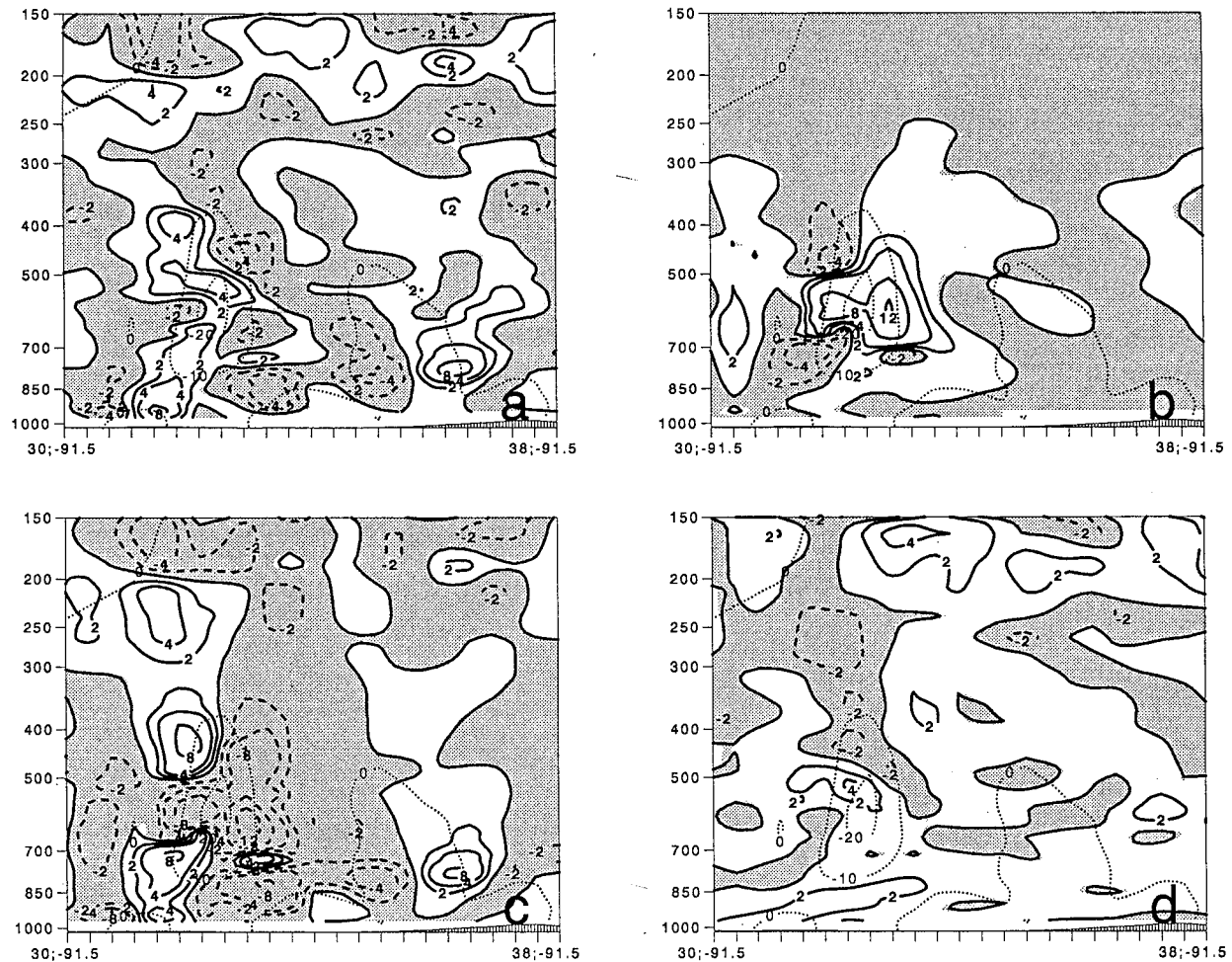
FIG. 13. Cross sections at 10 h through the area of maximum vertical motion. Vertical motion (dotted, 10×10^{-3} mb s^{-1} intervals) and frontogenetical forcings (positive solid, negative dashed and shaded, 1 K (100 km)$^{-1}$ (3h)$^{-1}$ intervals): (a) total, (b) condensational heating term D, (c) tilting term T, and (d) confluence term C.

any role in augmenting the intensification of the SWC, were not investigated.

6. Additional results

The modified Betts–Miller convective parameterization procedure is invoked in MESO if a parcel located in the 130-mb thick layer near the ground is conditionally unstable. The parcel with largest equivalent potential temperature in the 130-mb layer is used for evaluating convective condensation. It was noted in section 3a that the condensation in the SWC area is mostly due to resolvable scales. The base of convective clouds in midlatitudes in the real atmosphere is sometimes located at a high level close to 700 mb. It was therefore considered judicious to reintegrate MESO increasing the layer thickness from which a convective parcel may originate from 130 mb to 300 mb (nearly the thickness of SWC layer at 10 h in our case). We will refer to this

experiment as MESOC and the original integration as simply MESO in the following. It was anticipated that the above change in convective parametrization might generate upright parameterized convection from higher levels in MESOC, and might even induce upright vertical motions in the region where slanted vertical motions developed in the MESO integration. Slanted vertical motions also developed in MESOC. Thus, the development of the SWC in MESO is not affected by raising the level (from 130 to 300 mb) from which a parcel may originate in the convective parameterization scheme.

The data in the additional experiments described in this section were saved, as is normally the case, at 3 h intervals (see section 2). The impact of increasing the depth of the lowest layer from which parameterized convective clouds can originate was quite significant, especially in the nature of rainfall near front S. Rainfall amounts accumulated over 24 h from the initial time
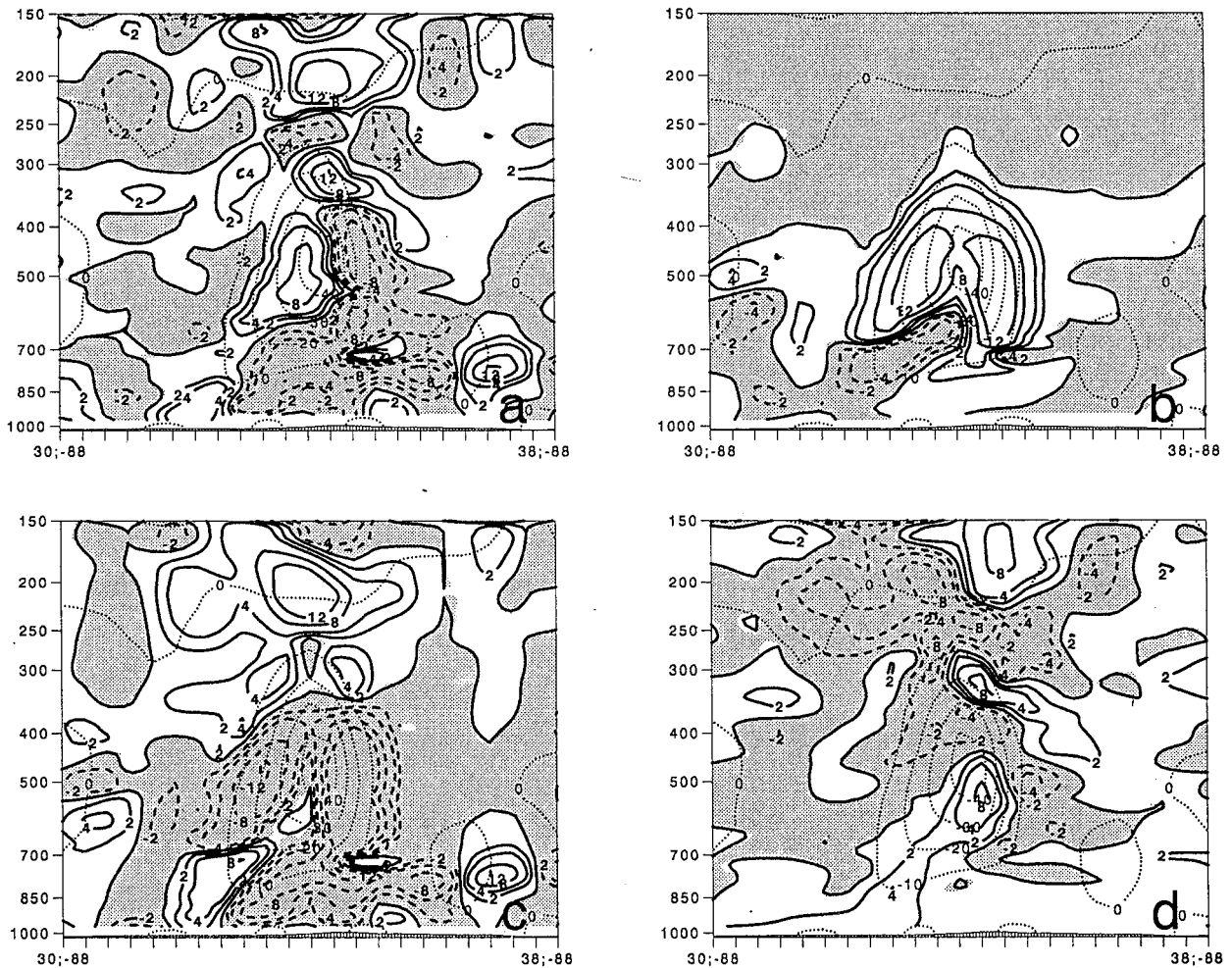
FIG. 14. Cross sections at 13 h through the area of maximum vertical motion. Vertical motion (dotted, 10×10^{-3} mb s^{-1} intervals) and frontogenetical forcings (positive solid, negative dashed and shaded, 1 K (100 km)$^{-1}$ (3h)$^{-1}$ intervals): (a) total, (b) condensational heating term D, (c) tilting term T, and (d) confluence term C.

were compared. The parameterized convective precipitation over the SWC region was negligible in MESOC, and absent in MESO. The area with resolvable-scale condensation exceeding 3 cm in the SWC region was larger in MESO than in MESOC. Maximum precipitation amounts along front S extending from southern Louisiana to southern Alabama were somewhat larger in MESO than in MESOC. In this region, the precipitation was mostly due to the parameterized convection in MESOC, whereas as can be seen from Figs. 1c–d both resolvable and parameterized convective rainfall occurred in MESO. Maximum vertical motion in the SWC area at 500 mb was weaker at 12 h in MESOC (-17×10^{-3} mb s^{-1}) than in MESO (-44×10^{-3} mb s^{-1}); and it was similar at 15 h in MESOC (-32×10^{-3} mb s^{-1}), and MESO (-35×10^{-3} mb s^{-1}). The maximum upward motion at 500 mb in the front S region was nearly the same in the two experiments, at both 12 and 15 h. The area with upward motion in the SWC

and front S regions was nearly the same in both experiments.

The resolvable-scale condensation over land in MESO is invoked at a RH greater than 0.75 (section 1). This criteria might be contributing to the development of SWC in MESO, since it allows condensation to occur at levels (especially higher levels) where the RH is much lower than 100% (see Fig. 7). The model was integrated setting the criteria for resolvable condensation to occur if RH exceeds 100% (experiment MESOR). The layer thickness from which a convective parcel can originate in MESOR was kept, as in MESOC, at 300 mb. The structure of slanted vertical motions was similar in MESOC and MESOR. Thus, the development of SWC does not depend on the value of RH (between 75% and 100%) above which resolvable-scale condensation is invoked.

As in MESOC, the parameterized convective precipitation over the SWC region was negligible in MESOR. Rainfall amounts (24-h accumulated) were somewhat

greater in MESOR than in MESOC over the SWC and front S areas. Parameterized convective precipitation amounts over the front S area were smaller in MESOR than in MESOC. The areal coverage and intensity of upward motion at 500 mb were similar in MESOR and MESOC over the SWC and front S areas, at both 12 and 15 h.

7. Concluding remarks

Data from NCEP's MESO model were utilized to investigate the evolution of slantwise convection in a weak frontal zone. Compared to some previous numerical (Bennetts and Sharp 1982; Lindstrom and Nordeng 1992; Zhang and Cho 1992) and observational (Sanders and Bosart 1985; Seltzer et al. 1985) studies on the development of slanted vertical motions, the data utilized in our study has a high uniform vertical (25 mb), and temporal (1 h), resolution. Although MESO utilizes a horizontal grid spacing of 29 km, the postprocessed data were available on a 40-km grid spacing; this horizontal resolution is comparable to those used in other numerical studies cited above. Use of high resolution, particularly in the vertical, allowed us to better delineate the zones with conditional and symmetric instabilities [see Persson and Warner (1991) for a discussion on consistent horizontal and vertical resolution for simulating CSI]. High temporal resolution allowed us to study in detail the time variation of various fields (sections 4–5), which provided insight into the frontogenetical and symmetrically unstable conditions that evolved in the region of slanted vertical motions.

Examination of the MESO forecast in the case presented in this paper and other cases suggests that the hydrostatic MESO model, without a CSI parameterization procedure included, simulates many features found in other observational and numerical studies of CSI. The slanted updrafts, a characteristic of CSI, are simulated explicitly. Slantwise vertical motions develop in the regions with negative moist potential vorticity and stable stratification. The condensational heating is associated with resolvable-scale motions and not with parameterized upright convection. The mesoscale vertical motion field develops into a single band with multiple embedded updrafts, aligned along the mean thermal wind direction. The buckling in the M surfaces is weaker than in the higher resolution nonhydrostatic models. The current horizontal resolution (29 km) is probably deficient in simulating the convective momentum transports; the buckling of M surfaces in some fine-mesh nonhydrostatic models arose mainly due to such transports (e.g., see Seman 1994). It is likely that this forecast of CSI would be improved if MESO's horizontal resolution is increased.

Development of strong slantwise vertical motions between 10 and 15 h discussed in the case investigated in this paper is attributed to a vertical coupling of a low-level CSI updraft with an upper-level convective updraft

(section 4). Initially a weak slanted updraft formed in a stably stratified shallow layer below 700 mb where conditional symmetrically unstable conditions prevailed (Figs. 6a and 8a). At the uppermost level of this CSI updraft conditionally unstable conditions existed and nearly upright upward motions developed. Resolvable-scale condensation occurred in both systems and the vertical motions intensified (Fig. 7). Initially the entire CSI updraft, as well as a portion of the upright updraft, contained negative moist potential vorticity (Fig. 8a). The negative MPV area was lifted upward, especially in areas where upward motion was stronger. As a result, the slanted motions extended upward to above 700 mb between 10 and 12 h. Maximum development occurred by 13 h when θ_e and M_g surfaces nearly coincided (Fig. 6c, section 4a). This adjustment to near-neutral conditions for slantwise convection takes place with the lifting and northward displacement of the negative MPV region away from the SWC area (Fig. 8c). Thus, both vertical and horizontal advection of MPV affect CSI updraft intensity.

The axis of maximum condensational heating becomes slanted in a fashion similar to the axis of vertical motion field in the SWC area (Fig. 7). Parameterized (vertical) convective condensation is nearly absent and condensation is mainly due to the resolvable scales in the SWC area. Another signature of slanted motions appears in the divergence field. The slanted axis of convergence (divergence) lies below (above) the axis of vertical motion (Fig. 10). The levels of maximum vertical motion, divergence, and convergence are displaced upward during the intensification phase of the slanted motions.

Strong pressure gradients and geostrophic winds (Fig. 11b) develop above 500 mb to the north (cool) side of the axis of maximum vertical motion mainly because of robust condensational heating gradients. Winds are subgeostrophic (Fig. 11a) in this region, however, due to the upward transport of low momentum from low levels (Fig. 12). Consequently, negative absolute vorticity values develop on the north side of the SWC in a deep layer (section 4b). The northward acceleration of winds in the inertially unstable region leads to the northward displacement of negative MPV, and northward extension of the CSI updraft and condensation (sections 4a, b).

The development of an elongated band aligned along the thermal wind direction (section 3b, Figs. 2c–d) is therefore likely an expression of conditional symmetric instability (see section 4). The slantwise motions promote frontogenesis along the warm side of the axis of maximum vertical motion at low levels, mainly due to an indirect circulation (section 5). The diabatic term is not included in some studies on frontogenesis because of nonavailability of condensational heating rates. Caution is warranted in interpreting results in such studies, because frontogenetical forcing due to the diabatic term can be very large in strong updraft regions (Fig. 14b).

REFERENCES

Antar, B. N., and W. W. Fowlis, 1983: Three-dimensional baroclinic instability of a Hadley cell. *J. Fluid Mech.,* **137,** 425–447.

Bennetts, D. A., and B. J. Hoskins, 1979: Conditional symmetric instability—A possible explanation of frontal rainbands. *Quart. J. Roy. Meteor. Soc.,* **105,** 945–962.

——, and J. C. Sharp, 1982: The relevance of conditional symmetric instability to the prediction of mesoscale frontal rainbands. *Quart. J. Roy. Meteor. Soc.,* **108,** 595–602.

Betts, A. K., and M. J. Miller, 1986: A new convective adjustment scheme. Part II: Single column tests using GATE wave, BOMEX and arctic air-mass data sets. *Quart. J. Roy. Meteor. Soc.,* **112,** 693–709.

Bjerknes, J., 1919: On the structure of moving cyclones. *Geofys. Publ.,* **1,** 1–8.

Blanchard, D. O., W. R. Cotton, and J. M. Brown, 1998: Mesoscale circulation growth under conditions of weak inertial instability. *Mon. Wea. Rev.,* **126,** 118–140.

Bluestein, H. B., 1986: Fronts and jet streaks: A theoretical perspective. *Mesoscale Meteorology and Forecasting,* P. S. Ray, Ed., Amer. Meteor. Soc., 173–215.

Bolton, D., 1980: The computation of equivalent potential temperature. *Mon. Wea. Rev.,* **108,** 1048–1053.

Bosart, L. F., and F. Sanders, 1986: Mesoscale structure in the Megalopolitan snowstorm of 11–12 February 1983. Part III: A large-amplitude gravity wave. *J. Atmos. Sci.,* **43,** 924–939.

Busse, F. H., and W. L. Chen, 1981: On the (nearly) symmetric instability. *J. Atmos. Sci.,* **38,** 877–880.

Carlson, T. N., 1991: *Mid-latitude Weather Systems.* HarperCollins Academic, 507 pp.

desJardins, M. L., K. F. Brill, S. Jacobs, S. S. Schotz, P. Bruehl, R. Schneider, B. Colman, and D. W. Plummer, 1996: N-AWIPS user's guide, version 5.4. National Centers for Environmental Prediction, Camp Springs, MD, 308 pp. [Available from NCEP/ NCO, W/NP14, Room 301, WWBG, NOAA, 5200 Auth Rd., Camp Springs, MD 20746-4304.]

——, S. Jacobs, D. Plummer, and S. Schotz, 1997: N-AWIPS: AWIPS at the National Centers for Environmental Prediction. Preprints, *13th Int. Conf. on Interactive Information and Processing Systems for Meteorology, Oceanography, and Hydrology,* Long Beach, CA, Amer. Meteor. Soc., 296–298.

Einaudi, F., W. L. Clark, D. Fua, J. L. Green, and T. E. VanZandt, 1987: Gravity waves and convection in Colorado during July 1983. *J. Atmos. Sci.,* **44,** 1534–1553.

Eliassen, A., 1959: The formation of fronts in the atmosphere. *The Atmosphere and the Sea in Motion,* B. Bolin, Ed., The Rockefeller Institute Press, 277–287.

Emanuel, K. A., 1979: Inertial instability and mesoscale convective systems. Part I. Linear theory of inertial instability. *J. Atmos. Sci.,* **36,** 2425–2449.

——, 1983a: The Lagrangian parcel dynamics of moist symmetric instability. *J. Atmos. Sci.,* **40,** 2368–2376.

——, 1983b: On assessing local conditional symmetric instability from atmospheric soundings. *Mon. Wea. Rev.,* **111,** 2016–2033.

——, 1985: Frontal circulations in the presence of small moist symmetric stability. *J. Atmos. Sci.,* **42,** 1062–1071.

Haltiner, G. J., and F. L. Martin, 1957: *Dynamic and Physical Meteorology.* McGraw-Hill, 470 pp.

Hoskins, B. J., and F. P. Bretherton, 1972: Atmospheric frontogenesis models: Mathematical formulation and solution. *J. Atmos. Sci.,* **29,** 11–37.

Janjic, Z. I., 1994: The step-mountain eta coordinate model: Further development of the convection, viscous sublayer, and turbulence closure schemes. *Mon. Wea. Rev.,* **122,** 927–945.

Kanamitsu, M., 1989: Description of the NMC global data assimilation and forecast system. *Wea. Forecasting,* **4,** 335–342.

Knight, D. J., and P. V. Hobbs, 1988: The mesoscale and microscale structure and organization of clouds and precipitation in mid-latitude cyclones. Part XV: A numerical modeling study of frontogenesis and cold-frontal rainbands. *J. Atmos. Sci.,* **45,** 915–930.

Koch, S. E., R. E. Golus, and P. J. Dorian, 1988: A mesoscale gravity wave event observed during CCOPE. Part II: Interactions between mesoscale convective systems and the antecedent waves. *Mon. Wea. Rev.,* **116,** 2545–2569.

Ley, B. E., and W. R. Peltier, 1978: Wave generation and frontal collapse. *J. Atmos. Sci.,* **35,** 3–17.

Lindstrom, S. S., and T. E. Nordeng, 1992: Parameterized slantwise convection in a numerical model. *Mon. Wea. Rev.,* **120,** 742–756.

Mathur, M. B., 1983: On the use of lower saturation criteria for release of latent heat in NWP models. *Mon. Wea. Rev.,* **111,** 1882–1885.

——, and M. Baldwin, 1995: Development of vertical and slantwise convection in ETA model's forecast for blizzard of 1993. *Proc. 10th Conf. on Numerical Weather Prediction,* Portland, OR, 108–109.

Mesinger, F., 1984: A blocking technique for representation of mountains in atmospheric models. *Riv. Meteor. Aeronaut.,* **44,** 195–202.

Miller, J. E., 1948: On the concept of frontogenesis. *J. Meteor.,* **5,** 169–171.

Miller, T. L., and B. N. Antar, 1986: Viscous nongeostrophic baroclinic stability. *J. Atmos. Sci.,* **43,** 329–338.

Molinari, J., and M. Dudek, 1992: Parameterization of convective precipitation in mesoscale numerical models: A critical review. *Mon. Wea. Rev.,* **120,** 326–344.

Newton, C. W., 1950: Structure and mechanism of the prefrontal squall line. *J. Meteor.,* **7,** 210–222.

Parsons, D. B., and P. V. Hobbs, 1983: The mesoscale and microscale structure and organization of clouds and precipitation in mid-latitude cyclones. Part XI: Comparisons between observational and theoretical aspects of rainbands. *J. Atmos. Sci.,* **40,** 2377–2399.

Persson, P. O. G., and T. T. Warner, 1991: Model generation of spurious gravity waves due to inconsistency of the vertical and horizontal resolution. *Mon. Wea. Rev.,* **119,** 917–935.

Reed, R. J., and F. Sanders, 1953: An investigation of the development of a mid-tropospheric frontal zone and its associated vorticity field. *J. Meteor.,* **10,** 338–349.

Rogers, E., T. L. Black, D. G. Deaven, and G. F. Dimego, 1996: Changes to the operational "Early" Eta analysis/forecast system at the National Centers for Environmental Prediction. *Wea. Forecasting,* **11,** 391–413.

Sanders, F., and L. F. Bosart, 1985: Mesoscale structure in the Megalopolitan snowstorm of 11–12 February 1983. Part I: Frontogenetical forcing and symmetric instability. *J. Atmos. Sci.,* **42,** 1050–1061.

Sawyer, J. S., 1956: The vertical circulation at meteorological fronts and its relation to frontogenesis. *Proc. Roy. Soc. London,* **234A,** 246–262.

Schneider, R. S., 1990: Large-amplitude mesoscale wave disturbances within the intense midwest extratropical cyclone of 15 December 1987. *Wea. Forecasting,* **5,** 533–558.

Seltzer, M. A., R. E. Passarelli, and K. A. Emanuel, 1985: The possible role of symmetric instability in the formation of precipitation bands. *J. Atmos. Sci.,* **42,** 2207–2219.

Seman, C. J., 1991: Numerical study of nonlinear convective-symmetric instability in a rotating baroclinic atmosphere. Ph.D. thesis, University of Wisconsin—Madison, 185 pp. [Available from

Dept. of Atmospheric and Oceanic Sciences, University of Wisconsin—Madison, Madison, WI 53706.]

——, 1994: A numerical study of nonlinear nonhydrostatic conditional symmetric instability in a convectively unstable atmosphere. *J. Atmos. Sci.,* **51,** 1352–1371.

Stobie, J. G., F. Einaudi, and L. W. Uccellini, 1983: A case study of gravity waves–convective storms interaction: 9 May 1979. *J. Atmos. Sci.,* **40,** 2804–2830.

Stone, P. H., 1966: On non-geostrophic baroclinic stability. *J. Atmos. Sci.,* **23,** 390–400.

——, 1970: On non-geostrophic baroclinic stability: Part II. *J. Atmos. Sci.,* **27,** 721–726.

Thorpe, A. J., and R. Rotunno, 1989: Nonlinear aspects of symmetric instability. *J. Atmos. Sci.,* **46,** 1285–1299.

Treadon, R. E., 1993: The NMC Eta Model post processor. A documentation. NMC Office Note 394, 44 pp. [Available from National Centers for Environmental Prediction, W/NP, Room 101, WWBG, NOAA, 5200 Auth Rd., Camp Springs, MD 20746-4304.]

Uccellini, L. W., and S. E. Koch, 1987: The synoptic setting and possible energy sources for mesoscale wave disturbances. *Mon. Wea. Rev.,* **115,** 721–729.

Wolfsberg, D. G., K. A. Emanuel, and R. E. Passarelli, 1986: Band formation in a New England winter storm. *Mon. Wea. Rev.,* **114,** 1552–1569.

Xu, Q., 1986: Conditional symmetric instability and mesoscale rainbands. *Quart. J. Roy. Meteor. Soc.,* **112,** 315–334.

Zhang, D.-L., and H. R. Cho, 1992: The development of negative moist potential vorticity in the stratiform region of a simulated squall line. *Mon. Wea. Rev.,* **120,** 1322–1341.

Zhao, Q., and F. H. Carr, 1997: A prognostic cloud scheme for operational NWP models. *Mon. Wea. Rev.,* **125,** 1931–1953.